

# Ordering and Fluctuation of Orbital and Lattice Distortion in Perovskite Manganese Oxides

Yukitoshi Motome

*Department of Physics, Tokyo Institute of Technology,  
Oh-okayama 2-12-1, Meguro-ku, Tokyo 152-8551*

Masatoshi Imada

*Institute for Solid State Physics, University of Tokyo,  
Roppongi 7-22-1, Minato-ku, Tokyo 106-8666  
(September 5, 2018)*

Roles of orbital and lattice degrees of freedom in strongly correlated systems are investigated to understand electronic properties of perovskite Mn oxides such as  $\text{La}_{1-x}\text{Sr}_x\text{MnO}_3$ . An extended double-exchange model containing Coulomb interaction, doubly degenerate orbitals and Jahn-Teller coupling is derived under full polarization of spins with two-dimensional anisotropy. Quantum fluctuation effects of Coulomb interaction and orbital degrees of freedom are investigated by using the quantum Monte Carlo method. In undoped states, it is crucial to consider both the Coulomb interaction and the Jahn-Teller coupling in reproducing characteristic hierarchy of energy scales among charge, orbital-lattice and spin degrees of freedom in experiments. Our numerical results quantitatively reproduce the charge gap amplitude as well as the stabilization energy and the amplitude of the cooperative Jahn-Teller distortion in undoped compounds. Upon doping of carriers, in the absence of the Jahn-Teller distortion, critical enhancement of both charge compressibility and orbital correlation length is found with decreasing doping concentration. These are discussed as origins of strong incoherence in charge dynamics. With the Jahn-Teller coupling in the doped region, collapse of the Jahn-Teller distortion and instability to phase separation are obtained and favorably compared with experiments. These provide a possible way to understand the complicated properties of lightly doped manganites.

PACS numbers: 71.30.+h, 71.27.+a, 71.20.Be, 71.38.+i

## I. INTRODUCTION

Perovskite Mn oxides show a variety of interesting physics depending on chemical composition and temperature. Pioneering work in 1950's revealed fascinating phase transitions from an antiferromagnetic insulator to a ferromagnetic metal.<sup>1–7</sup> The transitions take place through a change in the chemical composition which effectively introduces mobile holes in the systems. In 1970, a large negative magnetoresistance was discovered near the transition from the ferromagnetic metal to a paramagnetic state with increasing temperature.<sup>8,9</sup> Recently, this so-called colossal magnetoresistance has attracted renewed interest not only for understanding basic mechanisms but also for a possibility of technological applications.<sup>10</sup>

The basic physics in these systems has been examined by the so-called double-exchange mechanism.<sup>3</sup> In undoped states, each  $\text{Mn}^{3+}$  ion has four  $3d$  electrons in the  $(t_{2g})^3(e_g)^1$  configuration. Doped mobile holes are introduced to the twofold  $e_g$  orbitals. These situations have been examined based on the simplest version of the double-exchange (DE) model.<sup>3,6,7,11–13</sup> The model consists of noninteracting conduction electrons in a non-degenerate orbital and localized spins ferromagnetically coupled to this conduction band through the Hund's rule coupling.<sup>3</sup> The explicit form of the Hamiltonian is given by

$$\mathcal{H}_{\text{DE}} = \sum_{ij} \sum_{\sigma} t_{ij} c_{i\sigma}^{\dagger} c_{j\sigma} + K \sum_i \boldsymbol{\sigma}_i \cdot \mathbf{S}_i, \quad (1)$$

where  $c_{i\sigma}^{\dagger}$  ( $c_{i\sigma}$ ) creates (annihilates) a  $\sigma$ -spin electron at site  $i$ ;  $\boldsymbol{\sigma}_i$  is the spin operator for conduction electrons whereas  $\mathbf{S}_i$  denotes the localized spin at site  $i$ . This model successfully explains the metallic ferromagnetism under hole doping, the transition to paramagnetic phase with increasing temperature and the colossal magnetoresistance.

Recently, intensive experimental studies have revealed an importance of interplay among charge, spin, orbital and lattice degrees of freedom in the Mn oxides.<sup>10</sup> These systems show a Mott insulating or a charge-ordered state concomitant with spin, orbital and lattice orderings; a metallic state with different spin and orbital orderings; and various transitions between them. These novel phenomena strongly indicate a necessity for studies beyond the 'simple' DE model given by Eq. (1).

In particular, we discuss here the following experimental results which are difficult to understand within the 'simple' DE model: In undoped states, these materials are insulating with a charge gap of the order of 1eV. At low temperatures, this state shows spin, orbital and lattice orderings with strong two-dimensional (2D) anisotropy. The magnetic structure is called *A*-type and consists of ferromagnetic planes stacked antiferromagnetically. For instance, in  $\text{LaMnO}_3$ , the charge gap

amplitude  $\Delta_c$  is estimated around 1eV,<sup>14–17</sup> the transition to the 2D orbital-ordered state with lattice distortion (cooperative Jahn-Teller (JT) distortion) occurs at  $T_c \simeq 780\text{K}$ ,<sup>4,5,18–21</sup> and the *A*-type antiferromagnetic phase appears at  $T_N \simeq 140\text{K}$ .<sup>4,5,18</sup> These indicate a hierarchy structure of energy scales:  $\Delta_c \gg T_c \gg T_N$ .

When we dope holes, the materials show complex transitions at low temperatures; collapse of the JT distortion, magnetic and metal-insulator (MI) transitions.<sup>1,2,4,5,19,22–27</sup> Doped holes generally induce a spin canting; the spin direction in the 2D ferromagnetic planes tilts and a net ferromagnetic moment is induced without destroying the cooperative JT distortion.<sup>4,5,19,24,25</sup> Recently, neutron scattering experiment reported a charge or polaron ordering with 2D anisotropy around  $\delta = 0.125$  in the case of  $\text{La}_{1-x}\text{Sr}_x\text{MnO}_3$  (Sr concentration  $x$  corresponds to the hole concentration  $\delta$ ).<sup>26,27</sup> In this phase, the cooperative JT distortion is not observed whereas the spins are canted. The distortion collapses at  $\delta \simeq 0.1$ . The system remains insulating through the spin-canted state and finally at  $\delta \simeq 0.16$ , becomes the ferromagnetic metal.

An important and puzzling feature appears in the ferromagnetic state near the MI transition; in the case of  $\text{La}_{1-x}\text{Sr}_x\text{MnO}_3$ , for  $\delta \gtrsim 0.16$ . The metal exhibits strong charge incoherence at low temperatures where spin degrees of freedom are frozen up due to the perfect polarization. A strong mass enhancement is suggested by a small Drude weight  $D$  in the optical conductivity<sup>28,29</sup> and a small discontinuity at the Fermi edge in the photoemission spectra,<sup>30</sup> while there is no conspicuous enhancement in the specific heat coefficient  $\gamma$ .<sup>31</sup>

In order to consider the above experimental aspects, several approaches beyond the ‘simple’ DE model (1) have been explored. One is mean-field approximation. The undoped states have been investigated by effective Hamiltonian derived from a strong coupling limit of electron correlations,<sup>32–35</sup> by extended DE models with both spin and orbital degrees of freedom,<sup>36</sup> and by models containing oxygens.<sup>37,38</sup> These mean-field results commonly suggest energetic degeneracy between different spin and orbital structures. The importance of JT coupling or  $t_{2g}$ -spin interaction has been discussed to lift this degeneracy and to reproduce the realistic state. The following points, however, are missing in these calculations: They have not seriously considered the experimental energetic hierarchy,  $\Delta_c \gg T_c \gg T_N$ . Although the JT distortion appears in much higher energy scale than the spin ordering temperatures, the optimization of the ground state including phonons has not been successfully done. The model parameters, for instance, the interaction strength or the JT coupling they have chosen, are rather scattered and the consensus of parameter values is not reached. Among others, it should be noted that, as suggested in some degeneracy of various phases in these calculations, the magnetic and orbital structure must be under strong quantum fluctuations.

There is another approach, first-principles calculation,

which is applied mainly to undoped states. The local-density approximation (LDA) and the local-spin-density approximation (LSDA) conclude a gapless metal for the undoped state when the JT distortions are neglected. On the assumption of the experimental lattice structure, LSDA gives the antiferromagnetic insulator, although the charge gap amplitude is insufficient in reproducing the experimental result.<sup>39,40</sup> These are a consequence of the general tendency to underestimate electron correlation effects in these approximations. LDA+U calculations, in which the effects of strong correlation are taken into account by a Hartree-Fock scheme, have also been done under the experimental lattice structure and reproduced realistic values of the charge gap amplitude and the magnetic moment.<sup>39,41</sup> The improvement reached in LDA+U with the JT distortion implies that not only the JT coupling but also the strong correlation play an important role in these materials. The correct description of the experimentally-observed ground state, especially the large charge-gap amplitude, has not been reached ab initio. We note that it is rather hard to examine quantum fluctuation effects by the available band-structure calculations.

In contrast to the undoped states, doping effects have been less investigated theoretically. Especially, the JT distortions in doped regions have not been seriously examined. A systematic study on the doping effects is desired to discuss the collapse of the distortions and the charge or polaron ordering in experiments.

In the ferromagnetic metal, the strong charge incoherence has been discussed beyond the ‘simple’ DE models. Since the spins are perfectly polarized at low temperatures, this incoherence strongly suggests an importance of neglected elements in the model. Many candidates of the driving mechanism have been discussed such as JT fluctuation,<sup>42</sup> interorbital hopping of the  $e_g$  orbitals,<sup>43–45</sup> and strong Coulomb interaction.<sup>46</sup> Because the charge incoherence conspicuously appears near the MI transition, it is important to fully understand the undoped insulating states and to consider doping effects on them in a unified framework for treating quantum fluctuations.

In the present paper, ground state properties of the extended DE model containing the Coulomb interaction, twofold degeneracy of  $e_g$  orbitals, and the JT coupling are discussed. The undoped and doped states as well as critical properties of the MI transition are examined in a unified framework. A part of the results has been published in the previous publication.<sup>47,48</sup> In this paper, more systematic analyses are presented including the JT effects in hole-doped regions. As mentioned above, the real materials show strong 2D anisotropy at and around the undoped state, which suggests the importance of quantum fluctuations. The JT coupling to some extent suppresses these quantum fluctuations and plays a crucial role to reproduce experiments. In this work, the quantum fluctuation effects are investigated in the 2D anisotropic structure beyond the mean-field results; we use here an unbiased approach by employing the quantum Monte Carlo

method.<sup>49–51</sup> Effects of the JT distortion are also studied by optimizing the ground state of the Hamiltonian with an electron-phonon coupling. Physical properties in the optimized ground state are calculated and compared with the experimental results with emphasis on roles of the hierarchy structure in energy scales. We determine values of model parameters appropriate for the Mn compounds and compare with those in other theoretical calculations. For doping of carriers, critical enhancement of both orbital correlation length and charge compressibility is obtained in the absence of the JT distortion. The results are examined to understand the puzzling feature of the incoherent metal in experiments. We also show that the JT distortion rapidly becomes unstable with increasing doping. Phase separation takes place in our model when we take account of the JT coupling in the doped cases, which implies an instability to charge ordering in real materials.

This paper is organized as follows: In Sec. II, we describe derivation of our model and discuss the parameters used in the following discussions. Numerical results are presented in Sec. III. The numerical method and conditions are also described. All the results are discussed in comparison with experiments as well as with other theoretical studies in Sec. IV. Section V is devoted to summary.

## II. MODEL

In order to examine the above-mentioned experimental results beyond the ‘simple’ DE model defined in Eq. (1), we take account of on-site Coulomb interaction, twofold degeneracy of conduction bands, and JT coupling. Our Hamiltonian consists of three terms:<sup>47</sup>

$$\mathcal{H} = \mathcal{H}_{\text{el}} + \mathcal{H}_{\text{el-ph}} + \mathcal{H}_{\text{ph}}. \quad (2)$$

The first electronic term  $\mathcal{H}_{\text{el}}$  is derived from the extended DE model which contains the Coulomb interaction and two orbital degrees of freedom of  $e_g$  electrons as described in Sec. II A in detail. The second and third terms denote the electron-phonon interaction (JT coupling) and the elastic energy of phonons, respectively. Phonons are treated in a classical way as mentioned in Sec. II B. Section II C describes details of the model parameters used in the following calculations. In Sec. II D, the derivation of our model is examined to clarify energy scales and doping regions where our model can be applied.

### A. Electronic part

The extended DE model containing twofold degeneracy of  $e_g$  orbitals as well as on-site Coulomb interaction is given by

$$\mathcal{H}'_{\text{DE}} = \mathcal{H}_{\text{hop}} + \mathcal{H}_{\text{int}} + \mathcal{H}_K + \mathcal{H}_\mu, \quad (3)$$

where  $\mathcal{H}_{\text{hop}} = \sum_{ij,\nu\nu',\sigma} t_{ij}^{\nu\nu'} c_{i\nu\sigma}^\dagger c_{j\nu'\sigma}$  which describes electron hoppings;  $\mathcal{H}_{\text{int}}$  denotes on-site electronic interactions within doubly-degenerate  $e_g$  orbitals;  $\mathcal{H}_K$  is similar to the second term in Eq. (1) which describes the Hund’s rule coupling between electrons in the  $e_g$  orbitals and localized spins in the  $t_{2g}$  orbitals; and  $\mathcal{H}_\mu$  controls total electron density by the chemical potential  $\mu$ . The indices  $i, j = 1, \dots, N_s$  and  $\nu, \nu' = 1, 2$  denote the lattice sites of Mn atoms and the orbitals, respectively. We take  $\nu = 1(2)$  for the  $d_{x^2-y^2}(d_{3z^2-r^2})$  orbital. Although the  $t_{2g}$ -spin interaction such as  $\mathbf{S}_i \cdot \mathbf{S}_j$  has been considered in several previous studies,<sup>34–36</sup> it is ignored in Eq. (3) because the energy scale is small. This point will be discussed in Sec. II D.

Following several previous studies,<sup>6,7</sup> we consider the limit of the strong Hund’s-rule coupling,  $K|\mathcal{S}^{t_{2g}}| \gg t_{ij}^{\nu\nu'}$ , which may be appropriate for situations in many perovskite manganites. Since  $\sigma_i$  aligns parallel to  $\mathbf{S}_i$  in each site in this limit, the hopping integral between sites  $i$  and  $j$  is renormalized by a relative angle of the spins at sites  $i$  and  $j$ . Then the model (3) is simplified into a spinless fermion model as

$$\begin{aligned} \mathcal{H}'_{\text{DE}} \simeq & \sum_{ij,\nu\nu'} \lambda_{ij} t_{ij}^{\nu\nu'} c_{i\nu}^\dagger c_{j\nu'} \\ & + \tilde{U} \sum_i (n_{i1} - \frac{1}{2})(n_{i2} - \frac{1}{2}) + \mu \sum_{i,\nu} n_{i\nu}, \end{aligned} \quad (4)$$

where  $\lambda_{ij}$  is a renormalization factor determined by the expectation value of  $\mathbf{S}_i$  and  $\mathbf{S}_j$ ; and  $n_{i\nu} = c_{i\nu}^\dagger c_{i\nu}$  which denotes the number operator. Note that  $\tilde{U}$  is not a bare on-site Coulomb interaction but a renormalized one;  $\tilde{U} = U_{12} - J_{12}$  where  $U_{12}$  is the interorbital Coulomb interaction and  $J_{12}$  is the Hund’s rule coupling between the orbitals  $\nu = 1$  and  $2$ .

In undoped state where one electron occupies a site on average in the model (4) (we call this situation half filling hereafter), perovskite manganites commonly show the *A*-type antiferromagnetism. This state has strong 2D anisotropy attributed to antiferromagnetic stacking of ferromagnetic planes (*xy* planes).<sup>4,5,52</sup> When we dope holes, the system gradually recovers the three dimensionality and finally becomes an isotropic ferromagnetic metal through structural, magnetic and MI transitions.<sup>1,2,4,5,19,22–25</sup> However, the perfect polarization of spins in the 2D planes persists through these transitions; moreover, the 2D anisotropy remains for finite doping at least until the magnetic or the structural transition.<sup>4,5,19,22–27</sup> In this situation, the spin polarized model is well justified within the 2D plane without the *a posteriori* and ambiguous factor  $\lambda_{ij}$ .

On the basis of these considerations, here we consider the spin-polarized 2D model as a starting point to discuss physical properties of manganites at and around half filling. The explicit form of it is given by

$$\mathcal{H}_{\text{el}} = \sum_{ij,\nu\nu'} \tilde{t}_{ij}^{\nu\nu'} c_{i\nu}^\dagger c_{j\nu'}$$

$$+ \tilde{U} \sum_i (n_{i1} - \frac{1}{2})(n_{i2} - \frac{1}{2}) + \mu \sum_{i,\nu} n_{i\nu}. \quad (5)$$

Here we consider only the nearest-neighbor hopping integrals which are explicitly given by  $\tilde{t}_{ij}^{11} = -3\tilde{t}_0/4$ ,  $\tilde{t}_{ij}^{22} = -\tilde{t}_0/4$ ,  $\tilde{t}_{ij}^{12} = \tilde{t}_{ij}^{21} = -(+)\sqrt{3}\tilde{t}_0/4$  in the  $x(y)$  direction.<sup>53</sup> The unit of hopping integrals  $\tilde{t}_0$  is defined in Sec. II B. Our assumptions to derive Eq. (5) are examined in Sec. II D in detail.

### B. Jahn-Teller coupling

The  $Mn^{3+}$  ion has an instability of a distortion of  $MnO_6$  octahedron. This requires a strong electron-phonon coupling in the model, which is the so-called JT coupling.<sup>54</sup> There are two phonon modes which strongly couple with  $e_g$  orbital degrees of freedom.<sup>55,56</sup> In this work, lattice degrees of freedom are treated in a classical or adiabatic approximation, that is, kinetic energy of phonons is neglected.<sup>57,42</sup> Then, the Hamiltonian for this JT coupling is given in the form

$$\mathcal{H}_{\text{el-ph}} = -g \sum_i \mathbf{u}_i \cdot \mathbf{I}_i, \quad (6)$$

where  $g$  is the electron-phonon coupling constant;  $\mathbf{u}$  and  $\mathbf{I}$  are two-component vectors defined as

$$\mathbf{u}_i = u_i (\cos 2\theta_i, \sin 2\theta_i) \quad (7)$$

$$\mathbf{I}_i = 2(T_i^z, T_i^x), \quad (8)$$

where  $u_i$  denotes a displacement of the oxygens surrounding  $i$ -th Mn site and  $\theta_i$  is a coupling angle defined later in Eq. (11).  $T_i^\mu (\mu = x, y, z)$  is a pseudo-spin operator which denotes two degrees of freedom of the degenerate orbitals as

$$T_i^\mu = \frac{1}{2} \sum_{\nu\nu'} \boldsymbol{\tau}_{\nu\nu'}^\mu c_{i\nu}^\dagger c_{i\nu'}, \quad (9)$$

where  $\boldsymbol{\tau}$  is the Pauli matrix.

The term given by Eq. (6) is rewritten by substituting the definition (9) as

$$\mathcal{H}_{\text{el-ph}} = -g \sum_i u_i (m_{i1} - m_{i2}), \quad (10)$$

where  $m_{i\nu} \equiv \gamma_{i\nu}^\dagger \gamma_{i\nu}$  is the number operator for the new operator  $\gamma$  which is a linear combination of the operator  $c$  defined as

$$\begin{pmatrix} \gamma_{i1} \\ \gamma_{i2} \end{pmatrix} = \begin{pmatrix} \cos \theta_i & \sin \theta_i \\ -\sin \theta_i & \cos \theta_i \end{pmatrix} \begin{pmatrix} c_{i1} \\ c_{i2} \end{pmatrix}. \quad (11)$$

Then, Eq. (10) shows that the JT coupling in the classical approximation can be expressed as the local fields which lift the degeneracy of two orbitals diagonalized in the rotated basis by the coupling angle  $\theta_i$  as in Eq. (11).

The last term in the Hamiltonian (2) denotes the elastic energy of phonons as

$$\mathcal{H}_{\text{ph}} = k \sum_i u_i^2, \quad (12)$$

where  $k$  is the spring constant.

When an oxygen connecting  $i$  and  $j$ -th Mn sites is displaced by an amplitude  $u_i$ , the hopping integral between Mn sites,  $\tilde{t}_{ij}^{\nu\nu'}$ , is modulated since it originally consists of a product of hopping integrals between Mn and O sites. Note that in both the phonon modes considered here, oxygens shift only in the direction of Mn-O-Mn bonds. The Mn-O hopping is modified as  $(1 \pm 2u_i)^{-7/2}$  under the displacement of  $u_i$ <sup>58</sup> in the length unit mentioned in the next subsection Sec. II C. Therefore, we take the unit of Mn-Mn hopping integrals in Eq. (5) as

$$\tilde{t}_0 = t_0 (1 - 4u_i^2)^{-7/2}. \quad (13)$$

### C. Model parameters

We set  $t_0$  and the Mn-Mn lattice constant as the energy unit and the length unit, respectively. Our Hamiltonian contains the following parameters; the Coulomb interaction  $\tilde{U}$ , the electron-phonon coupling constant  $g$ , the spring constant  $k$ , and the parameters  $u_i$  and  $\theta_i$  which determine local JT distortions. From experiments and band calculations,<sup>14–17,39–41</sup>  $t_0$  is considered to be around 0.5eV and  $\tilde{U}$  is estimated as several eV. In this work,  $\tilde{U}/t_0$  is considered as a parameter in the following calculations. From our numerical results in Sec. III, the realistic value of  $\tilde{U}$  is discussed and compared with that in other theoretical investigations in Sec. IV. The spring constant  $k$  is roughly estimated from the frequency of an oxygen bond stretching phonon as the order of  $10 \sim 100$  eV; we use here  $k = 100$ .<sup>28,29,57</sup> The electron-phonon coupling constant  $g$  is hard to estimate from available experimental data. It may, however, be the order of 1eV; we take  $g = 10$  in this work. The values of  $k$  and  $g$  are examined in Sec. IV A by quantitative comparison between our results and experiments. The parameters  $u_i$  and  $\theta_i$  are determined to minimize the total energy. For simplicity, they are treated in a mean-field scheme as described in Sec. III B 2 in detail.

### D. Energy scale and doping range

In the following, the model given by Eq. (2) is considered in two dimensions. Here, we discuss the energy scale and the region of the doping concentration  $\delta$  where the present model is justified. In particular, two main simplifications in the model (5) are examined; one is neglect of three dimensionality and the other is the full polarization of spins. We also comment on the  $t_{2g}$ -spin exchange interaction neglected in Eq. (3).

In undoped states, the largest energy scale in our consideration is the charge gap  $\Delta_c$  of the order of 1eV. The formation of the gap is a common feature irrespective of the dimensionality. Therefore, physics of the charge gap formation in the energy scale of  $\Delta_c$  may well be captured in the 2D model equally to the isotropic 3D system.

When the energy scale is lowered below 1eV, the system becomes insulating and excitations are described through spin and orbital exchange processes because single-particle charge fluctuations are suppressed. Through these processes, the JT distortion and the orbital ordering take place in the energy scale of the order of 0.1eV. Although the interlayer structure of JT distortion and orbital ordering cannot be predicted, the energy scale of the distortion and the orbital ordering are again captured by the 2D model, because they take place in a planar configuration and the energy scale of these orderings may primarily be estimated from such anisotropic structure.

Although we employ a spin-polarized model, the spin configuration is not an important issue in this energy scale because the spin exchange energy is too small as compared to the above-mentioned energy scales. Whether spins are ordered or not does not make any crucial difference in our discussions.

With further lowering of the energy scale to the order of 0.01eV, a shortcoming of the spin-polarized 2D model becomes clear because the 3D spin ordering takes place under a competition of different possible 3D structures. We of course are not able to discuss such process. However, eventually, the *A*-type antiferromagnetic structure under the 2D anisotropic orbital ordering takes place, which again makes spin-polarized 2D model useful due to the strongly anisotropic structure with ferromagnetic alignment of spins in each plane at very low temperatures  $\sim 10$ K. We emphasize that the above energy hierarchy in undoped states provides the underlying backbone structure of this problem. Our model is useful in all the energy scales except those of the 3D spin-ordering process.

We neglect the  $t_{2g}$ -spin interaction in the starting DE model given by Eq. (3). The exchange coupling between nearest-neighbor  $t_{2g}$  spins is roughly estimated at the order of 0.001 or 0.01eV.<sup>5</sup> This energy scale is in the same order as the 3D magnetic transition temperature  $T_N$ . Actually, the  $t_{2g}$ -spin interaction is considered to be one of the origins of the *A*-type antiferromagnetism in undoped states.<sup>34-36</sup> Following the above discussions on the energy scales, we consider that the inclusion of this interaction term will not affect the essence of the following results in this paper.

Upon doping, a canted antiferromagnetic state is experimentally observed near the undoped state.<sup>4,19,24,25</sup> In this state, the perfect polarization of spins in each plane remains unperturbed, however, the direction of polarization tilts to the  $z$  direction. The canting angle increases with the increase in the doping concentration  $\delta$  and finally the isotropic ferromagnetic state appears with MI transition. This recovers the three dimensionality. When

we discuss the order-disorder transitions of the JT distortion and the orbital ordering, this 3D effect may be important.

We here estimate energy scales of the 3D effect by the spin canting. One is given by the transition temperature  $T_N$ . In  $\text{La}_{1-x}\text{Sr}_x\text{MnO}_3$ ,  $T_N$  does not strongly depend on the doping concentration and remains the order of 0.01eV through the spin-canted phase.

Another energy scale is kinetic energy in the  $z$  direction gained with the increase in the canting angle. We here estimate this energy gain following the work by de Gennes.<sup>7</sup> He analyzed the DE model (1) by mean-field approximation to explain the origin of spin-canted phase observed by neutron scattering experiment for  $\text{La}_{1-x}\text{Ca}_x\text{MnO}_3$ . If his formalism is applied straightforwardly, roughly speaking, the kinetic-energy gain of each hole increases linearly with the canting angle and hence linearly with the doping concentration. Then, the total kinetic-energy gain is estimated as

$$\Delta E_t^z \simeq -\frac{(\tilde{t}^{22})^z}{\delta_m} \delta^2, \quad (14)$$

for  $0 < \delta \lesssim \delta_m$  where  $\delta_m$  is the critical concentration for the ferromagnetic transition. In the case of  $\text{La}_{1-x}\text{Sr}_x\text{MnO}_3$ , the transition occurs at  $\delta_m \simeq 0.16$ .<sup>24,25</sup> In terms of our model,  $(\tilde{t}^{22})^z$  is equal to  $-\tilde{t}_0$ .

In order to discuss the 2D anisotropic structure of the JT distortion and the orbital ordering in the energy scales smaller than  $T_N$  or  $\Delta E_t^z$  in doped states, the three dimensionality should be taken into account. In other words, our 2D model may be useful to discuss these ordering processes in the energy scales larger than  $T_N$  or  $\Delta E_t^z$  even at finite hole doping.

In the metallic state with further doping, if we assume that the MI transition is a continuous or a weak first-order one, there is a critical region of  $\delta$  where the system is controlled by the criticality of the transition. In the real materials, the insulators show the 2D anisotropy in both the orbital ordering and the JT distortion. The metallic state near the MI transition may be influenced by the 2D anisotropy of the insulator.<sup>46</sup> Our 2D model would serve to discuss the criticality of the MI transition.

### III. RESULTS

This section presents numerical results for the model (2) in the ground state. First, Sec. III A describes numerical technique and details of computational conditions. Then in Sec. III B, we show numerical results at half filling without and with the JT coupling. Results for hole-doped cases are presented in Sec. III C. All the results are discussed in comparison with experiments as well as with other theoretical investigations in Sec. IV.

## A. Method and computational details

We investigate ground state properties of the model (2) by the projection quantum Monte Carlo (PQMC) method.<sup>49–51</sup> If JT distortions are given, that is, if the parameters  $u_i$  and  $\theta_i$  are fixed, the Hamiltonian given by Eq. (2) is the Hubbard model with a generalized hopping and external fields. Therefore we can apply a well-established algorithm for the ordinary single-band Hubbard model straightforwardly.<sup>59,60,49–51</sup> In two dimensions, quantum fluctuations may be important even in insulating states. PQMC gives unbiased results on the effects of electron correlation and quantum fluctuations.

For simplicity, the JT coupling given by Eq. (6) is treated in a mean-field scheme. As described in Sec. III B 2, we fix  $\theta_i$  following the experimental indications and find a uniform solution  $u_i = u$  to minimize total energy by PQMC.

For the present model, PQMC has the so-called negative sign problem even at half filling with  $g = 0$ , although this problem is completely absent for the ordinary Hubbard model at half filling.<sup>59,60</sup> However, from practical point of view, we have managed to reach the ground-state convergence in several choices of parameter values. Physical quantities presented in the following are obtained in the parameter region where the negative sign problem is not serious in reaching the ground state properties with needed accuracy. The details are discussed in Appendix A.

In PQMC, ground states are projected out by operating  $\exp(-\beta\mathcal{H})$  on a trial wave function. For good convergence about the projection  $\beta$ , we employ several different trial wave functions depending on the cases; noninteracting Slater determinant, unrestricted Hartree-Fock solutions,<sup>61</sup> and orbital-singlet wave functions stabilized by small dimerization in hoppings.<sup>62</sup> The convergence for these trial wave functions is discussed in Appendix A. Discreteness  $\Delta\tau$  of the slices in the projection  $\beta$  is taken as  $\Delta\tau t_0 = 0.05$  which is small enough to obtain ground state properties within numerical errorbars.

The 2D systems with  $N_S = L^2$  sites are investigated in the following. As shown in Appendix B, we note that this model defined on a finite-size lattice shows different behavior depending on the linear dimension  $L = 4n$  or  $4n + 2$  ( $n$  is an integer) as well as on boundary conditions due to the shapes of Fermi surfaces in the finite-size systems. In extrapolations to the thermodynamic limit  $N_S \rightarrow \infty$ , we pay attention to choose a suitable set of  $L$  and the boundary condition to reduce finite-size effects. In the following, we mainly show the results for a series of  $L = 4n$  with the antiperiodic boundary condition and  $L = 4n + 2$  with the periodic boundary condition. See Appendix B for details.

## B. Half filling

### 1. Without Jahn-Teller coupling

First, the ground states at half filling are investigated in the absence of the JT coupling. The system becomes Mott insulating for finite values of the Coulomb interaction  $\tilde{U}$ . In the following, we show numerical results on the charge gap amplitude and the orbital ordering at this filling.

Figure 1 shows the system-size dependence of the charge gap amplitude for various values of the Coulomb interaction  $\tilde{U}$ . Here, the charge gap is calculated from the shift of the chemical potential when we dope holes to the half-filled state.<sup>63</sup> The data for each value of  $\tilde{U}$  are well fitted by  $1/L$  as in the ordinary single-band Hubbard model.<sup>63,64</sup>

Figure 2 summarizes the charge gap amplitude in the thermodynamic limit obtained by the extrapolations in Fig. 1. For comparison, we plot the QMC results for the ordinary Hubbard model<sup>64</sup> as well as the results of the mean-field approximations for both models. The QMC data on the present model show remarkable reduction of the charge gap amplitude in the region of  $\tilde{U}$  considered here in comparison with the mean-field results as well as the QMC result in the ordinary Hubbard model. This means that quantum fluctuations may be more important in the present model than in the ordinary Hubbard model. Although further studies are necessary to discuss the value of  $\tilde{U}$  for the opening of the gap, increasing the Coulomb interaction  $\tilde{U}$  opens the charge gap and let the system be Mott insulating; however in order to reproduce the realistic values of charge gap amplitude ( $\Delta_c \sim 2t_0$ ) only with  $\tilde{U}$  without the JT coupling, it is necessary to take much larger interaction than  $\tilde{U} = 5$ .

The Mott insulating state induced by the Coulomb interaction shows a staggered orbital ordering. We calculate the orbital correlation function defined as

$$T^\mu(\mathbf{k}) = N_S^{-1} \sum_{ij} T_i^\mu T_j^\mu \exp(i\mathbf{k} \cdot \mathbf{r}_{ij}) \quad (15)$$

with the operator given by Eq. (9) ( $\mu = x, y, z$ ). For a finite value of  $\tilde{U}$ ,  $T^x(\mathbf{k})$  shows a peak at  $\mathbf{k} = \mathbf{Q} \equiv (\pi, \pi)$  as shown in Fig. 3, while  $T^y(\mathbf{k})$  and  $T^z(\mathbf{k})$  do not have a conspicuous structure.

The moment of this staggered orbital ordering is calculated by  $M^x = [T^x(\mathbf{Q})/N_S]^{1/2}$ . Figure 4 plots the system-size dependence of the staggered moment  $M^x$ . The data are well fitted by  $1/L$ , from which we obtain the results in the thermodynamic limit summarized in Fig. 5. We also plot in the figure the QMC result for the antiferromagnetic spin-ordering moment in the ordinary Hubbard model<sup>49</sup> and the mean-field results as in Fig. 2. In small  $\tilde{U}$  region, the moment grows slower than the mean-field results as the charge gap amplitude in Fig. 2, however it grows rapidly around  $\tilde{U} = 4$ ; this may be related to the uniaxial property of the moment in the present model. Actually, in numerical calculations for small clusters,<sup>65</sup> the moment in our model grows rapidly

and is saturated to its full value  $M^x = 1/2$  for large values of  $\tilde{U}$ ; on the other hand, the isotropic moment in the ordinary Hubbard model slowly approaches a reduced value because of stronger quantum fluctuations.

For the following discussions, we consider here the pattern of the orbital ordering. Our model exhibits a staggered ordering of  $(|d_{x^2-y^2}\rangle + |d_{3z^2-r^2}\rangle)/(|d_{x^2-y^2}\rangle - |d_{3z^2-r^2}\rangle)$  type indicated by the peak structure of  $T^x(\mathbf{Q})$ . If we define a single-site state by the linear combination of the two orbitals as

$$|\psi(\phi_i)\rangle = |d_{x^2-y^2}\rangle \cos \phi_i + |d_{3z^2-r^2}\rangle \sin \phi_i, \quad (16)$$

the ordering pattern is characterized by  $\phi_i = (-1)^{|\mathbf{r}_i^x + \mathbf{r}_i^y|} \pi/4$ . See Fig. 6. The previous mean-field studies have predicted slightly different patterns from our results,  $\phi_i \simeq (-1)^{|\mathbf{r}_i^x + \mathbf{r}_i^y|} \pi/3$ .<sup>32,33,35-38</sup> We will discuss this discrepancy as a 3D effect in Sec. IV A 2.

### 2. With Jahn-Teller coupling

Next, effects of the JT coupling at half filling are investigated. In experiments, the cooperative JT distortions are observed with 2D anisotropy whose ordering pattern is characterized by

$$\theta_i = (-1)^{|\mathbf{r}_i^x + \mathbf{r}_i^y|} \pi/6 \quad (17)$$

with a uniform amplitude of  $u \sim 0.035$  in terms of Eq. (6).<sup>20</sup> Following these results, we treat here lattice degrees of freedom in a mean-field scheme for simplicity; we fix  $\theta_i$  as Eq. (17), and optimize the total energy by PQMC to determine a uniform solution of  $u$ .

Figure 7 illustrates these procedures. We change the values of  $u$  and calculate the total energy by PQMC to find the optimized ground state. In the figures, the data at  $N_S = \infty$  are obtained by extrapolations by using the size scaling relation  $E_g(L) \simeq E_g(L = \infty) + aL^{-3}$  based on the spin-wave theory,<sup>66,49</sup> as exemplified in Fig. 8. For each value of  $\tilde{U}$ , the total energy is considerably lowered by introducing JT distortions and the data are well fitted by

$$E_g(u) \simeq E_g(u = 0) - E_{JT} + a(u - u^*)^2 \quad (18)$$

near the minimum, where  $E_{JT}$  is the stabilization energy of the JT distortion and  $u^*$  is the optimized amplitude of oxygen displacement. The data on  $E_{JT}$  and  $u^*$  are summarized in Fig. 11 and will be discussed below.

The JT distortions reduce quantum fluctuations and stabilize the insulating states. We calculate the charge gap amplitude for the optimized states at  $u = u^*$ . The JT coupling given by Eq. (6) breaks the particle-hole symmetry at half filling, therefore we calculate the charge gap for both electron doping ( $\Delta_c^+$ ) and hole doping ( $\Delta_c^-$ ). Here, the charge gap is calculated from the imaginary-time dependence of uniform single-particle Green's functions defined as  $G(\mathbf{r}_{ij} = 0, \tau) \equiv \sum_\nu G_\nu(\mathbf{r}_{ij} = 0, \tau)$  with

$$G_\nu(\mathbf{r}_{ij}, \tau) = \Theta(\tau) \langle \Psi_0 | c_{i\nu}(\tau) c_{i\nu}^\dagger | \Psi_0 \rangle - \Theta(-\tau) \langle \Psi_0 | c_{i\nu}^\dagger(\tau) c_{i\nu} | \Psi_0 \rangle, \quad (19)$$

where  $|\Psi_0\rangle$  is the normalized ground state at half filling and  $\Theta(\tau)$  is the step function. The recently-developed stable algorithm is applied to obtain  $G(\tau)$  for the large values of the imaginary time  $|\tau|$ .<sup>64</sup> The results of  $G(\tau)$  are shown in Fig. 9 for the case of  $\tilde{U} = 3$  as an example. The exponential fits to the tails of  $G(\tau > 0)$  ( $G(\tau < 0)$ ) give the values of the charge gap  $\Delta_c^+$  ( $\Delta_c^-$ ). Figure 10 shows the system-size dependence of the charge gap amplitude obtained from the fits in Fig. 9. The extrapolation in the  $1/L$  dependence gives the data in the thermodynamic limit. The amplitudes of the charge gap are remarkably enhanced by the JT distortions from the values in Fig. 2.

Figure 11 summarizes our results on the half-filled states in the presence of both the Coulomb interaction and the JT coupling. We plot the stabilization energy of the JT distortion  $E_{JT}$ , the amplitude of the oxygen displacement  $u^*$ , and the charge gap amplitude  $\Delta_c^\pm$  as a function of the Coulomb interaction  $\tilde{U}$ . The corresponding values in experiments on LaMnO<sub>3</sub> are also shown for comparison: For the stabilization energy  $E_{JT}$ , we show the ordering temperature of orbital and lattice  $\simeq 780$ K.<sup>4,5,18,21</sup> The temperature is not exactly the same quantity as  $E_{JT}$ , however it is useful to compare these quantities at least in their orders of magnitude. This point will be discussed later in Sec. IV A 1. For the oxygen displacement  $u^*$ , we cite X-ray experiment which gives  $u^* \simeq 0.035$ .<sup>20</sup> For the charge gap amplitude, we show the experimental value  $\Delta_c \simeq 1$ eV obtained by the optical conductivity.<sup>16</sup> As shown in Figs. 11(a)-(c), these experimental results are consistently reproduced in our calculations for the value of  $\tilde{U} \simeq 4$  or 5, although slight adjustment on  $\tilde{U}$ ,  $g$  or  $k$  is required for more quantitative argument. For instance, if we take  $k = 130$  at  $\tilde{U} = 5$  and  $g = 10$ , as shown in Fig. 11, we obtain more quantitative agreement between the numerical data and the experimental values. These results will be discussed in Sec. IV A 1 in more detail.

The JT coupling with the angle of Eq. (17) changes the orbital-ordering pattern. Figure 12 shows the angle of the pattern,  $\phi_i$  defined in Eq. (16), as a function of  $u$ . The angle  $|\phi_i|$  is calculated from the moments of orbital polarizations,  $M^x$  and  $M^z$ , in the form

$$|\phi_i| = \frac{1}{2} \arctan \left( \frac{M^x}{M^z} \right), \quad (20)$$

which is easily confirmed by the definition (16). Note that the case of  $u = 0$  corresponds to the result in Sec. III B 1, that is,  $|\phi_i| = \pi/4$ . For the large values of  $u$ , the angle  $|\phi_i|$  approaches  $\pi/6$  which equals to  $|\theta_i|$  in Eq. (17). In the case of  $\tilde{U} = 4$ ,  $g = 10$ , and  $k = 100$ , the angle  $|\phi_i|$  is around  $\pi/5$  for  $u^* \simeq 0.0475$ . See also Fig. 6. This result will be compared with experiments in Sec. IV A 2.

### C. Hole doping

#### 1. Without JT coupling

In the following, the results of doped states are presented. Carrier doping leads to an MI transition. In the absence of the JT coupling, the metal near the Mott transition shows some anomalous behavior in our 2D model.

The first anomaly appears in the charge compressibility. Figure 13 shows the doping-concentration dependence of the chemical potential  $\mu$ . Here, in order to reduce the finite-size effects,  $\mu$  is calculated from the energy difference between adjacent closed-shell configurations.<sup>63</sup> The chemical potential  $\mu$  has a jump at  $\delta = 0$  due to the finite Mott gap and changes continuously in the doped region. The monotonic decrease of  $\mu$  with increasing  $\delta$  suggests that there is no phase separation in our 2D model without the JT coupling. As shown in Fig. 13(b), the chemical potential scales to  $\delta^2$  near the MI transition at  $\delta = 0$ . This indicates that the compressibility  $\kappa \equiv dn/d\mu$  diverges as

$$\kappa \propto \delta^{-1} \quad (21)$$

toward the transition.

Another anomaly is the critical enhancement of the orbital short-ranged correlations. In the doped region, the orbital correlation is enhanced by the Coulomb interaction. Figure 14 shows the doping dependence of the peak values of the orbital correlation function defined in Eq. (15) for various values of the interaction  $\tilde{U}$ . For finite values of  $\tilde{U}$ , the correlation shows a diverging behavior towards the undoped state where the orbital correlation is long-ranged. This behavior becomes more conspicuous with increasing the value of  $\tilde{U}$ .

Figure 15 summarizes the data on the orbital correlations at  $\tilde{U} = 4$  for various system sizes. The inverse peak values are plotted in this figure. The data are independent of system sizes even near  $\delta = 0$ , which indicates that the orbital correlations are short-ranged. As shown in this plot, we find a scaling relation given by

$$T^x(\mathbf{Q}) \propto \delta^{-1} \quad (22)$$

in the vicinity of the MI transition. This suggests that the orbital ordering at  $\delta = 0$  is immediately destroyed by hole doping and that the short-ranged correlation diverges towards the transition in the doped region.

These anomalous properties are in marked contrast with the usual MI transition from a metal to a band insulator. The scaling relations, Eqs. (21) and (22), are similar to those in the ordinary single-band Hubbard model in two dimensions.<sup>63</sup> This similarity is discussed in Sec. IV B 1 to characterize the MI transition in the present model. Our results will be examined to consider the charge incoherence in experiments.

#### 2. With JT coupling

Here, the effects of the JT coupling in hole-doped region are investigated. Phonons are treated by the mean-field approximation as in Sec. III B 2. The mean-field treatment generally overestimates the JT distortion especially in doped cases since it neglects various fluctuations. Actually, Fig. 16(a) shows that the cooperative JT distortion remains finite in a wide range of doping.

However the stabilization energy of the JT distortion decreases rapidly as a function of the doping concentration  $\delta$ . Figure 16(b) shows  $\delta$  dependence of the stabilization energy of the JT distortion. The rough estimates of the cutoff energy are also shown in the figure, below which some other energy scales not considered in our model come into play as discussed in Sec. II D; one is the magnetic transition temperature  $T_N$  for  $\text{La}_{1-x}\text{Sr}_x\text{MnO}_3$ ,<sup>25</sup> and the other is the effect of 3D hoppings  $\Delta E_t^z$  given by Eq. (14). In Sec. IV B 2, the collapse of the JT distortion will be discussed with this rapid decrease of  $E_{\text{JT}}$ .

Figure 17(a) shows doping dependence of the ground state energy per site  $E_g$  at  $\tilde{U} = 4$  in the presence of the JT coupling. The data show a convex region close to half filling.

In order to see this behavior more clearly, we consider the quantity in each system size defined by

$$E_g^* = E_g - E_g(\delta = 0) - \Delta_c^* \delta, \quad (23)$$

where  $\Delta_c^*$  is the slope of  $E_g$  at  $\delta = 0$  in Fig. 17(a) and represents the charge gap amplitude obtained as the chemical potential in the closed-shell adjacent to half filling. Figure 17(b) plots doping dependence of  $E_g^*$ . The convex behavior is clearly seen near the half-filled state. It becomes more conspicuous with increasing the system size.

The convex region of  $E_g$  as a function of doping indicates an instability to phase separation. The region of the phase separation is determined by a tangent drawn from the point at  $\delta = 0$  to the curve of  $E_g$  in Fig. 17(a) or equivalently  $E_g^*$  in Fig. 17(b). States which have a higher energy than this line in the convex region are unstable and replaced by ones on the line with phase mixing. The phase mixture consists of the half-filled state and a doped state at which the tangent line comes in contact with the energy curve.

In the present model, the phase separation takes place between the half-filled state with the cooperative JT distortion and the doped metallic state, although it is difficult to determine the critical doping concentration in this case of  $\tilde{U} = 4$ . Within the mean-field treatment, the latter doped state is still accompanied by the JT distortion as shown in Fig. 16(a). In Sec. IV B 3, these results will be examined in detail, especially to understand the charge-ordered state in experiments. They will also be compared with other theoretical studies.

## IV. DISCUSSION

In this section, we discuss our numerical results shown in the previous section. For the half-filled states, the synergetic effects between the Coulomb interaction and the JT coupling are clarified in Sec. IV A 1. Our results are compared with experiments on perovskite Mn oxides as well as with other theoretical investigations. The pattern of orbital ordering is examined in Sec. IV A 2. In Sec. IV B, numerical results in the hole-doped states are discussed in comparison with the recent experiments. The critical properties of the MI transition, especially effects of orbital fluctuations, are examined in Sec. IV B 1 as origins of the experimentally-observed charge incoherence. Doping effects in the presence of the JT distortions are also discussed to understand experiments in lightly doped region. We consider the collapse of the JT distortions in Sec. IV B 2 and the phase separation in Sec. IV B 3.

### A. Undoped state

#### 1. Synergy of Coulomb interaction and JT coupling

Consider first the case that we take account of only the Coulomb interaction and neglect the JT coupling. As shown in Sec. III B 1, the system becomes Mott insulating with the staggered orbital ordering. The charge gap opens much slower than the mean-field results, which shows the mean-field approximation is not appropriate due to strong quantum fluctuations in the region of  $\tilde{U}$  considered here. We speculate that the somewhat complicated nesting property discussed in Appendix B may be related to this strong fluctuation.

This strong fluctuation effect is also inferred from in the previous studies. Several mean-field analyses predicted energetic degeneracy between different spin and orbital structures.<sup>32,33,35–38</sup> Larger values of  $\tilde{U}$  are required than that in our estimates ( $\tilde{U} \simeq 4–5$ ) to reproduce experimental results because they have not taken into account large contribution from the JT coupling. Note also that in LDA and LSDA calculations which generally tend to underestimate the electron correlation effects, a ferromagnetic metal would be realized if the JT distortion is absent.<sup>39,40</sup>

On the other hand, if only the JT coupling is taken into account, we obtain a cooperative JT distortion with an orbital ordering; however, as shown in Fig. 11, the JT distortion is too small to reproduce the realistic oxygen distortions and the charge gap amplitude. This shortcoming may correspond to the insufficient charge-gap amplitude predicted in LSDA using the experimental JT distortions.<sup>39,40</sup>

When the effects of both the Coulomb interaction and the JT coupling are considered as in Sec. III B 2, the experimental results on charge, orbital, and lattice degrees of freedom are quantitatively reproduced within the

present model. Our finding of the synergetic effect by the electron correlation and the JT coupling suggests that the value of  $\tilde{U}$  around 4 or 5 would be sufficient to reproduce experimental results. Our results give a consistent picture of the energetic hierarchy in the undoped state: (i) The charge gap of the order of 1eV opens as the consequence of the synergy between the on-site Coulomb interaction and the atomic JT coupling. These two elements work cooperatively and nonlinearly. (ii) The correlations of the orbital and the lattice distortion grow in the energy scale one order of magnitude smaller than the charge gap amplitude. The transition temperature of these orderings is around 0.1eV. (iii) The two elements which are neglected in our model, that is, the three dimensionality and spin degrees of freedom, may not be relevant to understand the experimental results considered here. The 3D antiferromagnetic state of *A*-type appears at the energy much smaller than the above two energy scales, namely, at the order of 0.01eV. Orbital and lattice states may not be much affected by the magnetic ordering.

In our analyses, the Coulomb interaction is considered in an unbiased way in PQMC, while the lattice distortions are treated in the mean-field scheme. Therefore, the effects of the interaction on the orbital correlations are fully taken into account up to the short-ranged and dynamical fluctuations, whereas such fluctuations of the JT distortions are neglected. This will lead to the following consequence: The charge gap amplitude,  $\Delta_c$ , could be overestimated since the formation of a polaron is not considered. A doped hole in the insulator may cause a relaxation of the JT distortion around it to form a polaron. Therefore, the charge gap may decrease due to the formation energy of the polaron. For the precise estimate of  $\Delta_c$  under this effect, it is necessary to fully take into account of the local JT distortions.

Another point to be discussed in our analyses is the comparison between the stabilization energy of the JT distortion  $E_{JT}$  and the transition temperature  $T_c$  of the orbital and lattice orderings. To be precise,  $E_{JT}$  is the energy difference between the JT-distorted state and the undistorted one with the orbital ordering stabilized by the Coulomb interaction. It contains not only the intersite-correlation energy of the orbital and lattice orderings but also the on-site JT polarization energy. On the other hand, the transition temperature  $T_c$  should be basically determined by the intersite correlations of the orbital and lattice orderings<sup>54</sup> because the on-site JT polarization may already be more or less stabilized well above  $T_c$ . Therefore, in our results,  $E_{JT}$  may overestimate the energy scale of  $T_c$ .

The above two points presumably require larger values of parameters,  $\tilde{U}$ ,  $g$ , or  $k$  than in the present work. We need further studies on the JT fluctuation effects and also on a more appropriate choice of the parameter values.

## 2. Pattern of orbital ordering

First, consider the pattern of the orbital ordering determined only by the Coulomb interaction. As described in Sec. III B 1, our 2D model shows the pattern with  $\phi_i = (-1)^{|\mathbf{r}_i^x + \mathbf{r}_i^y|} \pi/4$  in terms of Eq. (16), which is slightly different from the previous mean-field results in 3D models as shown in Fig. 6. In order to understand this discrepancy, we discuss here effects of the three dimensionality neglected in our 2D model. In the  $z$  direction, the hopping integral has a strong orbital dependence; whose explicit form is given by  $\tilde{t}_{ij}^{11} = \tilde{t}_{ij}^{12} = \tilde{t}_{ij}^{21} = 0$  and  $\tilde{t}_{ij}^{22} = -\tilde{t}_0$ . This favors larger occupation of the  $d_{3z^2-r^2}$  orbital in 3D systems than in 2D since only the  $d_{3z^2-r^2}$  orbital has an overlap to the  $z$  direction. Therefore, we expect that the orbital-ordering pattern obtained in the present work, that is,  $(|d_{x^2-y^2}\rangle + |d_{3z^2-r^2}\rangle) / (|d_{x^2-y^2}\rangle - |d_{3z^2-r^2}\rangle)$  type may be modified in a way that a uniform component of  $d_{3z^2-r^2}$  increases. In other words, our result  $|\phi_i| = \pi/4$  gives a lower bound for the angle  $|\phi_i|$  in the 3D models. The resultant ordering may look like  $|d_{z^2-x^2}\rangle / |d_{y^2-z^2}\rangle$  type. See Fig. 6. Actually, this type of orbital ordering was obtained by the mean-field approximation for 3D electron systems.<sup>32,33,35-38</sup>

When the JT coupling is taken into account, as shown in Fig. 12, the lattice distortion modifies the orbital ordering. Our result at  $\tilde{U} = 4$  gives  $|\phi_i| \simeq \pi/5$ , which is very close to  $|d_{3x^2-r^2}\rangle / |d_{3y^2-r^2}\rangle$ -type. Since our calculations neglect the three dimensionality, the angle  $|\phi_i| \simeq \pi/5$  may give a lower bound as discussed above.

Recently, the staggered orbital ordering in  $\text{LaMnO}_3$  was experimentally observed by the resonant X-ray scattering technique,<sup>21</sup> although this experiment has not succeeded in determining the angle  $|\phi_i|$  unfortunately. In principle, the angle  $|\phi_i|$  can be determined from the intensity of the fundamental reflection in this experiment.<sup>67</sup> More detailed experiments are desired to compare our numerical results.

## B. Doped state

### 1. Incoherence in charge dynamics

Here, the critical properties of the MI transition in our 2D model are analyzed in the absence of the JT coupling. As mentioned in Sec. III C 1, the metal shows two anomalous properties near the MI transition; the critical divergence of both the compressibility and the orbital short-ranged correlation. In the 2D ordinary Hubbard model, the same scaling relations as Eqs. (21) and (22) have been reported in detailed numerical investigations.<sup>63</sup> The scaling theory based on the hyperscaling hypothesis describes this MI transition with the novel universality class characterized by  $z = 1/\nu = 4$ ,<sup>68</sup> where  $z$  is the dynamical exponent and  $\nu$  is the correlation-length exponent. Recently, other anomalies in this MI transition have also

been found in the localization length in the insulating state<sup>69</sup> and the flat dispersion near  $\mathbf{k} = (\pi, 0)$ .<sup>70</sup> These two also support the scaling statement. The scaling relations in our model, Eqs. (21) and (22), imply that the MI transition in the present model is in a similar universality class to the ordinary Hubbard model.

This argument may give a clue to understand the strong charge incoherence near the MI transition observed in perovskite Mn oxides.<sup>28,29</sup> In the ordinary Hubbard and  $t$ - $J$  models, the optical conductivity has been numerically investigated to clarify the strong incoherence in charge dynamics.<sup>71,72</sup> In these models, the residual entropy and the spin short-ranged correlations are enhanced towards the MI transition point, which may be the origin of such charge incoherence. The role of spins in these models is replaced with orbital degrees of freedom in the present model (5). This suggests that the orbital correlations induced by the Coulomb interaction may be one of the driving mechanisms of the experimentally-observed charge incoherence. Actually, we have also calculated the optical conductivity in the present model by the exact diagonalization of small clusters and obtained strongly incoherent properties as expected. These results will be reported elsewhere in detail.<sup>73</sup>

Experimentally, the incoherent charge dynamics is observed not only in the 3D materials but also in the 2D ones such as  $\text{La}_{2-2x}\text{Sr}_{1+2x}\text{Mn}_2\text{O}_7$  near  $x = 0.4$ .<sup>74</sup> This fact suggests that the essence of the charge incoherence in these materials is captured by the models of metals near the MI transition from strongly 2D anisotropic insulators. The scaling argument assuming such an anisotropy in energy dispersions has been discussed recently by one of the authors.<sup>46</sup> It implies that the system has a 2D anomalous dispersion with a flat  $\mathbf{k}$ -dependence caused by the critically-enhanced 2D orbital correlations. This argument provides one possible scenario to reconcile the puzzling situations in the 3D materials which were mentioned in Sec. I; the specific-heat coefficient  $\gamma$  remains small and is not critically enhanced<sup>31</sup> while the Drude weight  $D$  and the discontinuity at the Fermi edge are strongly suppressed in the critical region.<sup>28-30</sup> Our results support the existence of the 2D anomalous dispersion in the charge excitation near the Mott transition in the present model. To confirm this scenario further, it is necessary to investigate the  $\mathbf{k}$ -dependence of the dispersion directly. This is left for future study.

### 2. Collapse of JT distortion

In real materials, the cooperative JT distortions persist up to finite doping concentration in the spin-canted state, for instance, up to  $\delta \simeq 0.1$  in  $\text{La}_{1-x}\text{Sr}_x\text{MnO}_3$ .<sup>24,25</sup> In our results in Sec. III C 2, although the JT distortion loses its stability rapidly with increasing the doping concentration, it remains finite in a wide range of doping. This presumably results from the mean-field treatment in

which the fluctuations of the JT distortions are neglected. The doped holes may form polarons, which leads to an importance of the so-called breathing mode of phonons.<sup>57</sup> Therefore, the short-ranged JT fluctuations should be taken into account more seriously in the doped region than in the undoped state. To precisely estimate the doping concentration where the JT distortion collapses, it is necessary to fully consider the JT fluctuations.

Since the distortion has strong 2D anisotropy, the three dimensionality may also be important to understand the collapse of the JT distortion. In Fig. 16(b), the energy scales discussed in Sec. II D are plotted for comparison; the magnetic transition temperature  $T_N$  and the kinetic-energy gain by the three dimensionality,  $\Delta E_t^z$ . Our model may not be appropriate to discuss phenomena happening in the energy scale comparable to them. In order to consider the JT distortion for  $\delta \gtrsim 0.1$  where  $E_{\text{JT}}$  becomes comparable to  $\Delta E_t^z$ , we may need to include 3D effects.

The above two points require further studies on doping effects with the JT distortions. The former, the fluctuation effects of the JT distortions, may be partly taken into account within the present model (2) if we fully optimize the parameters  $u_i$  and  $\theta_i$ .

### 3. Phase separation

Our results in the doped region with the JT coupling indicate the existence of the phase separation. This phase separation is a consequence of two factors; one is the critically-enhanced compressibility which exists even in the absence of the JT coupling as in Eq. (21), and the other is the large stabilization energy  $E_{\text{JT}}$  which decreases rapidly with increasing doping. Therefore, even if the JT fluctuation effects are taken into account, the phase separation may persist in the present model.

In real systems, the additional elements such as the long-ranged Coulomb interaction might be crucial to replace the phase separation by another instability, for instance, an ordering of the hole distribution. Recently, the charge ordering has been reported in  $\text{La}_{1-x}\text{Sr}_x\text{MnO}_3$  around  $x = 0.125$ .<sup>26,27</sup> From neutron-scattering data, this phase has been interpreted as a stacking of two alternating layers; one has little hole with a similar JT distortion to the undoped state, and the other contains excess holes and shows no apparent JT distortion. This phase is favorably compared to our result of the phase separation because it predicts the phase mixture of the JT-distorted undoped state and the doped one. The latter doped phase may show no apparent JT distortion if we take account of the JT fluctuations as mentioned in Sec. IV B 2.

Recently, the phase separation has also been discussed in the original ‘simple’ DE model given by Eq. (1).<sup>77–79</sup> In these studies, the system shows the phase separation between an undoped antiferromagnetic insulator and a

doped ferromagnetic metal at low temperatures. Effects of the JT distortion on this phase separation have also been discussed.<sup>80</sup> In these cases, the phase separation originates from a change in the density of states between two states; the antiferromagnetic insulator stabilized by superexchange interaction has a narrow band while the ferromagnetic metal dominated by the DE interaction has a rather wide band. Note that in the ‘simple’ DE model, the phase separation takes place even in the absence of the Coulomb interaction between the conduction electrons. On the other hand, in our model, the Coulomb interaction plays a crucial role to induce the phase separation as mentioned above.

### 4. Remark

Our numerical results may give a comprehensive scenario to understand the complicated properties in lightly-doped Mn oxides: Doped holes induce the JT fluctuations. The spin canting enhances the 3D motions of doped holes. These may contribute cooperatively to collapse the cooperative JT distortion which becomes unstable rapidly at a small doping concentration. On the other hand, the critical region of the MI transition may be wider than the critical concentration of the collapse. Note that the critical region of the Mott transition spreads up to  $\delta \simeq 0.2 - 0.3$  in the case of  $\tilde{U} = 5$  as shown in Fig. 13(b). Then, the doped state beyond the collapse of the JT distortion shows the strong incoherence in charge dynamics. In these lightly-doped regions, charge degrees of freedom have an instability suggested by the phase separation in our results. At a commensurate filling, for instance, at  $\delta = 0.125 = 1/8$ , doped holes may form a hyperlattice structure as indicated in experiments.

## V. SUMMARY

In this work, roles of orbital and lattice degrees of freedom in the extended double-exchange models have been investigated to understand remarkable properties of undoped and lightly-doped perovskite Mn oxides. The models contain the Coulomb interaction, double degeneracy of the conduction bands and the Jahn-Teller coupling. The ground state properties are studied under full polarization of spins with two-dimensional anisotropy by using the quantum Monte Carlo method. Fluctuation effects of Coulomb interaction and orbital degrees of freedom are investigated without biased approximations.

In the undoped states, the importance of both the Coulomb interaction and the Jahn-Teller coupling is clarified. In the absence of the Jahn-Teller coupling, the system shows strong quantum fluctuations with remarkable suppression of the Mott gap amplitude. A realistic amplitude of the Jahn-Teller coupling suppresses the fluc-

tuations and stabilizes the insulating state. Synergy between the Coulomb interaction and the Jahn-Teller coupling remarkably enhances the charge gap amplitude and reproduces the realistic Jahn-Teller distortion. Our numerical results give us a consistent picture of the undoped states, especially of the characteristic hierarchy of energy scales among charge, orbital-lattice, and spin degrees of freedom. The energy hierarchy consists of the charge gap  $\sim 1\text{eV}$ , orbital and lattice ordering energy  $\sim 0.1\text{eV}$ , and spin ordering and 3D coupling scales  $\sim 0.01\text{eV}$ . The pattern of staggered orbital orderings has also been investigated in detail. It would be desired to compare it with more detailed experiments in the future.

Upon doping of carriers, the critical properties of the metal-insulator transition have been investigated in the absence of the Jahn-Teller distortion. Our numerical results show two anomalies; the critical enhancement of the compressibility and the orbital short-ranged correlations towards the transition. These results are analyzed by using the scaling argument in comparison with the ordinary Hubbard model. The orbital fluctuation enhanced by the Coulomb interaction is discussed as one of the driving mechanisms of the strong incoherence in charge dynamics observed in experiments.

Next, the effects of the Jahn-Teller coupling in the hole-doped region have been investigated. Our mean-field treatment of phonons suggests that the cooperative Jahn-Teller distortion becomes unstable rapidly with increasing hole doping. Moreover, the instability of phase separation appears near the undoped state. These results are favorably compared with the collapse of the Jahn-Teller distortion and the charge-ordered phase observed in experiments. We propose a scenario to understand the rich physics of the lightly-doped Mn oxides; the order-disorder Jahn-Teller transition, the charge ordering near the magnetic and metal-insulator transition, and the strong charge incoherence. More detailed study on fluctuation effects of the Jahn-Teller distortions as well as on the three dimensionality is left for further study.

## ACKNOWLEDGEMENT

The authors thank Junjiro Kanamori and Hiroki Nakano for fruitful discussions. A part of the computations in this work was performed by using the facilities of the Supercomputer Center, Institute of Solid State Physics, University of Tokyo. This work is supported by ‘Research for the Future Program’ from Japan Society for Promotion of Science (JSPS-RFTF 97P01103). Y. M. acknowledges the financial support of Research Fellowships of Japan Society for the Promotion of Science for Young Scientists.

## APPENDIX A:

In this Appendix, we discuss the negative sign problem in PQMC for the model given by Eq. (5). The ratio of the negative sign in QMC sampling depends on the system size  $N_S$ , the Coulomb interaction  $\tilde{U}$ , the trial wave function, and the doping concentration  $\delta$ .<sup>75,76</sup>

First, it should be pointed out that PQMC for the present model shows negative-sign samples even at the particle-hole symmetric point, that is, at half filling ( $\mu = 0$ ). In contrast to this, for the ordinary Hubbard model, the negative sign problem completely disappears at half filling;<sup>59,60</sup> the system is mapped to an attractive Hubbard model under the transformations as

$$c_{i\uparrow}^\dagger \rightarrow (-1)^i \tilde{c}_{i\uparrow}, \quad c_{i\downarrow}^\dagger \rightarrow \tilde{c}_{i\downarrow}^\dagger, \quad (A1)$$

which ensure the positivity of samples in QMC. This mapping does not apply to the present model (5) because of the difference in the diagonal hoppings,  $t^{11} \neq t^{22}$ , and the off-diagonal elements  $t^{12}, t^{21}$ . This leads to the negative sign problem even at half filling.

Figures 18-20 show  $\beta$  dependence of the expectation value of the sign of the MC samples,  $\langle S \rangle$ , at half filling. In the figures,  $\beta$  is the projection parameter; the ground state is projected out by the operation of  $\exp(-\beta\mathcal{H})$  on a trial wave function. As shown in Figs. 18 and 19, larger system size or larger interaction makes the negative sign problem more serious.

Figure 20 indicates that it is important to choose an appropriate trial state in decreasing the sign problem. In the present work, the half-filled cases are studied by using the unrestricted Hartree-Fock solutions and the non-interacting Slater determinant or the orbital-singlet wave functions depending on the values of  $\tilde{U}$ . The unrestricted Hartree-Fock solutions are optimized with the value of the interaction  $\tilde{U}$  used in the Hartree-Fock calculations to give the best convergence as shown in Fig. 22 later.<sup>61</sup> The orbital-singlet wave functions are given by the system with a tiny dimerization introduced in the hopping integrals to ensure that the ground state is singlet.<sup>62</sup>

Figure 21 shows  $\delta$  dependence of  $\langle S \rangle$  at  $\beta = 5$ . We note that  $\langle S \rangle$  has the largest value at half filling. The negative sign problem becomes severe in the lightly doped region,  $0 < \delta \lesssim 0.5$ . For the doped cases, we use the noninteracting Slater determinant or the orbital-singlet wave functions as the trial state.

The convergence of physical quantities with increasing  $\beta$  strongly depends on the choice of trial wave functions. As an example, Fig. 22 shows the peak value of the orbital correlation function at half filling. In this case, a fast convergence is obtained if we control the input value of  $\tilde{U}$  in the unrestricted Hartree-Fock calculations.<sup>61</sup> Generally, the choice of input  $\tilde{U}$  somewhat less than the value of the interaction in the model makes the fastest convergence. This may be related to the large deviations of the QMC results from the mean-field ones

due to the strong quantum fluctuations discussed in Sec. III B 1.

## APPENDIX B:

Here, the noninteracting case ( $\tilde{U} = 0$ ) in the 2D model (5) is discussed. We show the energy dispersions of this model and Fermi surfaces at half filling which have a perfect nesting property. We also discuss the boundary conditions and finite-size effects in the linear dimension  $L$  of the system. These considerations are helpful for systematic analyses of numerical results in Sec. III.

By Fourier transformation, the hopping matrix  $\tilde{t}_{ij}^{\nu\nu'}$  for  $u_i = 0$  in Eq. (5) is denoted as

$$\varepsilon^{\nu\nu'}(\mathbf{k}) = \varepsilon_0(\mathbf{k})\delta_{\nu\nu'} + \varepsilon_1(\mathbf{k})\tau_{\nu\nu'}^z + \varepsilon_2(\mathbf{k})\tau_{\nu\nu'}^x, \quad (\text{B1})$$

where  $\delta_{\nu\nu'}$  is the Cronecker's delta function and  $\tau^\mu$  is  $\mu$  component of the Pauli matrix. Here we define

$$\varepsilon_0 = -t_0(\cos k_x + \cos k_y) \quad (\text{B2})$$

$$\varepsilon_1 = -t_0/2(\cos k_x + \cos k_y) \quad (\text{B3})$$

$$\varepsilon_2 = \sqrt{3}t_0/2(\cos k_x - \cos k_y). \quad (\text{B4})$$

The  $2 \times 2$  matrix  $\varepsilon^{\nu\nu'}(\mathbf{k})$  is easily diagonalized to derive energy dispersions in the form

$$\varepsilon_{\pm} = \varepsilon_0 \pm \sqrt{\varepsilon_1^2 + \varepsilon_2^2}, \quad (\text{B5})$$

which are shown in Fig. 23.

At half filling, we obtain the Fermi surfaces shown in Fig. 24. Note that they satisfy a perfect nesting condition, that is,  $\mathbf{k}(\varepsilon_+ = 0) = \mathbf{k}(\varepsilon_- = 0) + \mathbf{Q}$ , where  $\mathbf{Q} = (\pi, \pi)$ . Therefore, we expect that the system may become an insulator when we switch on the interaction  $\tilde{U}$ .

It should be stressed that the Fermi surface in Fig. 24 has many different ways of nesting. Besides the above-mentioned nesting with the wave vector  $\mathbf{Q}$  between two different branches, it is possible to nest the Fermi surfaces in the same branch with wave vectors  $(\pi, a)$  or  $(a, \pi)$  where  $a$  is an arbitrary number between 0 and  $\pi$ . In addition, the nesting between different branches with  $(\pi, a)$  or  $(a, \pi)$  is also possible. Therefore, our 2D model (5) may have a competition between these various nestings at half filling, which may lead to the strong quantum fluctuations as seen in numerical results in Sec. III B 1.

At half filling, finite-size systems with  $N_S = L^2$  sites are divided in two different series depending on a linear dimension  $L$  and boundary conditions: One is a group which has  $\mathbf{k}$ -points on the Fermi surfaces and the other does not have. In other words, the former has gapless but the latter has finite gap excitations in noninteracting cases. The former is a series in which  $L = 4n$  ( $n$  is an integer) with the periodic boundary conditions or  $L = 4n + 2$  with the antiperiodic boundary conditions,

and the latter is  $L = 4n$  with the antiperiodic boundary conditions or  $L = 4n + 2$  with the periodic boundary conditions.

These two series should be independently extrapolated to the thermodynamic limit  $N_S \rightarrow \infty$ . Figure 25 shows these extrapolations of the ground state energy. The extrapolated values in two series agree well within the errorbars. In Sec. III, numerical calculations and extrapolations to the thermodynamic limit are carefully done by considering these different series separately.

In the doped cases, in order to reduce finite-size effects, we consider mainly the electron fillings at which the closed-shell configuration is satisfied in the noninteracting case.<sup>63</sup> As seen in Sec. III C 1 and III C 2, especially for the calculations of the chemical potential, this procedure works well and gives a smooth  $\delta$  dependence insensitive to the system sizes except for the phase-separated region.

---

<sup>1</sup> G. H. Jonker and J. H. Van Santen, Physica **16**, 337 (1950).  
<sup>2</sup> J. H. Van Santen and G. H. Jonker, Physica **16**, 599 (1950).  
<sup>3</sup> C. Zener, Phys. Rev. **82**, 403 (1951).  
<sup>4</sup> E. O. Wollan and W. C. Koehler, Phys. Rev. **100**, 545 (1955).  
<sup>5</sup> J. B. Goodenough, Phys. Rev. **100**, 564 (1955).  
<sup>6</sup> P. W. Anderson and H. Hasegawa, Phys. Rev. **100**, 675 (1955).  
<sup>7</sup> P. G. de Gennes, Phys. Rev. **118**, 141 (1960).  
<sup>8</sup> C. W. Searle and S. T. Wang, Can. J. Phys. **48**, 2023 (1970).  
<sup>9</sup> C. W. Searle and S. T. Wang, Can. J. Phys. **47**, 2703 (1969).  
<sup>10</sup> A. P. Ramirez, J. Phys. Cond. Matter. **9**, 8171 (1997), and references therein.  
<sup>11</sup> K. Kubo and N. Ohata, J. Phys. Soc. Jpn. **33**, 21 (1972).  
<sup>12</sup> N. Furukawa, J. Phys. Soc. Jpn. **63**, 3214 (1994).  
<sup>13</sup> For a recent review see, N. Furukawa, preprint (cond-mat/9812066).  
<sup>14</sup> A. E. Bocquet *et al.*, Phys. Rev. B **46**, 3771 (1992).  
<sup>15</sup> A. Chainani, M. Mathew, and D. D. Sarma, Phys. Rev. B **47**, 15397 (1993).  
<sup>16</sup> T. Arima, Y. Tokura, and J. B. Torrance, Phys. Rev. B **48**, 17006 (1993).  
<sup>17</sup> T. Saitoh *et al.*, Phys. Rev. B **51**, 13942 (1995).  
<sup>18</sup> G. Matsumoto, J. Phys. Soc. Jpn. **29**, 606 (1970).  
<sup>19</sup> G. Matsumoto, J. Phys. Soc. Jpn. **29**, 615 (1970).  
<sup>20</sup> J. B. A. A. Ellemans, B. van Laar, K. R. van der Veer, and B. O. Loopstra, J. Solid State Chem. **3**, 328 (1971).  
<sup>21</sup> Y. Murakami *et al.*, Phys. Rev. Lett. **81**, 582 (1998).  
<sup>22</sup> Y. Tokura *et al.*, J. Phys. Soc. Jpn. **63**, 3931 (1994).  
<sup>23</sup> A. Urushibara *et al.*, Phys. Rev. B **51**, 14103 (1995).  
<sup>24</sup> H. Kawano, R. Kajimoto, M. Kubuta, and H. Yoshizawa, Phys. Rev. B **53**, 2202 (1996).  
<sup>25</sup> H. Kawano, R. Kajimoto, M. Kubuta, and H. Yoshizawa,

Phys. Rev. B **53**, 14709 (1996).

<sup>26</sup> Y. Yamada, O. Hino, S. Nohdo, and R. Kanao, Phys. Rev. Lett. **77**, 904 (1996).

<sup>27</sup> J.-S. Zhou, J. B. Goodenough, A. Asamitsu, and Y. Tokura, Phys. Rev. Lett. **79**, 3234 (1997).

<sup>28</sup> Y. Okimoto *et al.*, Phys. Rev. Lett. **75**, 109 (1995).

<sup>29</sup> Y. Okimoto *et al.*, Phys. Rev. B **55**, 4206 (1997).

<sup>30</sup> D. D. Sarma *et al.*, Phys. Rev. B **53**, 6873 (1996).

<sup>31</sup> B. F. Woodfield, M. L. Wilson, and J. M. Byers, Phys. Rev. Lett. **78**, 3201 (1997).

<sup>32</sup> K. I. Kugel' and D. I. Khomskii, Sov. Phys. JETP **37**, 725 (1973).

<sup>33</sup> R. Shiina, T. Nishitani, and H. Shiba, J. Phys. Soc. Jpn. **66**, 3159 (1997).

<sup>34</sup> S. Ishihara, J. Inoue, and S. Maekawa, Phys. Rev. B **55**, 8280 (1997).

<sup>35</sup> L. F. Feiner and A. M. Oleś, Phys. Rev. B **59**, 3295 (1999).

<sup>36</sup> R. Maezono, S. Ishihara, and N. Nagaosa, Phys. Rev. B **57**, 13993 (1998).

<sup>37</sup> T. Mizokawa and A. Fujimori, Phys. Rev. B **51**, 12880 (1995).

<sup>38</sup> T. Mizokawa and A. Fujimori, Phys. Rev. B **54**, 5368 (1996).

<sup>39</sup> S. Satpathy, Z. S. Popović, and F. R. Vukojlović, Phys. Rev. Lett. **76**, 960 (1996).

<sup>40</sup> I. Solovyev, N. Hamada, and K. Terakura, Phys. Rev. Lett. **76**, 4825 (1996).

<sup>41</sup> I. Solovyev, N. Hamada, and K. Terakura, Phys. Rev. B **53**, 7158 (1996).

<sup>42</sup> A. J. Millis, R. Mueller, and B. I. Shraiman, Phys. Rev. B **54**, 5405 (1996).

<sup>43</sup> H. Shiba, R. Shiina, and A. Takahashi, J. Phys. Soc. Jpn. **66**, 941 (1997).

<sup>44</sup> P. E. Brito and H. Shiba, Phys. Rev. B **57**, 1539 (1998).

<sup>45</sup> A. Takahashi and H. Shiba, Euro. Phys. Journal. B **5**, 413 (1998).

<sup>46</sup> M. Imada, J. Phys. Soc. Jpn. **67**, 45 (1998).

<sup>47</sup> Y. Motome and M. Imada, J. Phys. Soc. Jpn. **68**, 16 (1999).

<sup>48</sup> Y. Motome, H. Nakano, and M. Imada, preprint (cond-mat/9811221).

<sup>49</sup> S. R. White *et al.*, and R. T. Scaletter, Phys. Rev. B **40**, 506 (1989).

<sup>50</sup> M. Imada and Y. Hatsugai, J. Phys. Soc. Jpn. **58**, 3752 (1989).

<sup>51</sup> S. Sorella, Int. J. Mod. Phys. B **5**, 937 (1991).

<sup>52</sup> K. Hirota, N. Kaneko, A. Nishizawa, and Y. Endoh, J. Phys. Soc. Jpn. **65**, 3736 (1996).

<sup>53</sup> P. W. Anderson, Phys. Rev. **115**, 2 (1959).

<sup>54</sup> J. Kanamori, J. Appl. Phys. **31**, 14S (1960).

<sup>55</sup> J. H. Van Vleck, J. Chem. Phys. **7**, 472 (1939).

<sup>56</sup> J. B. Goodenough, *Magnetism and Chemical Bond* (John Wiley & Sons, New York, London, 1963).

<sup>57</sup> A. J. Millis, Phys. Rev. B **53**, 8434 (1996).

<sup>58</sup> W. A. Harrison, *Electronic Structure and the Properties of Solids, The Physics of the Chemical Bond* (W. H. Freeman and Company, San Francisco, 1980).

<sup>59</sup> J. E. Hirsch, Phys. Rev. B **28**, 4059 (1983).

<sup>60</sup> J. E. Hirsch, Phys. Rev. B **31**, 4403 (1985).

<sup>61</sup> N. Furukawa and M. Imada, J. Phys. Soc. Jpn. **60**, 3669 (1991).

<sup>62</sup> F. F. Assaad, M. Imada, and D. J. Scalapino, Phys. Rev. B **56**, 15001 (1997).

<sup>63</sup> N. Furukawa and M. Imada, J. Phys. Soc. Jpn. **61**, 3331 (1992).

<sup>64</sup> F. F. Assaad and M. Imada, J. Phys. Soc. Jpn. **65**, 189 (1996).

<sup>65</sup> H. Nakano, private communication.

<sup>66</sup> D. A. Huse, Phys. Rev. B **37**, 2380 (1988).

<sup>67</sup> S. Ishihara and S. Maekawa, Phys. Rev. B **58**, 13442 (1998).

<sup>68</sup> M. Imada, J. Phys. Soc. Jpn. **64**, 2954 (1995).

<sup>69</sup> F. F. Assaad and M. Imada, Phys. Rev. Lett. **76**, 3176 (1996).

<sup>70</sup> M. Imada, F. F. Assaad, H. Tsunetsugu, and Y. Motome, preprint (cond-mat/9808044).

<sup>71</sup> H. Nakano and M. Imada, J. Phys. Soc. Jpn. (to be published).

<sup>72</sup> H. Tsunetsugu and M. Imada, J. Phys. Soc. Jpn. **67**, 1864 (1998).

<sup>73</sup> H. Nakano, Y. Motome, and M. Imada, unpublished.

<sup>74</sup> T. Ishikawa, T. Kimura, T. Katsufuji, and Y. Tokura, Phys. Rev. B **57**, 8079 (1998).

<sup>75</sup> E. Y. Loh *et al.*, Phys. Rev. B **41**, 9301 (1990).

<sup>76</sup> N. Furukawa and M. Imada, J. Phys. Soc. Jpn. **60**, 810 (1991).

<sup>77</sup> S. Yunoki *et al.*, Phys. Rev. Lett. **80**, 845 (1998).

<sup>78</sup> E. Dagotto *et al.*, Phys. Rev. B **58**, 6414 (1998).

<sup>79</sup> S. Yunoki and A. Moreo, Phys. Rev. B **58**, 6403 (1998).

<sup>80</sup> S. Yunoki, A. Moreo, and E. Dagotto, preprint (cond-mat/9807149).

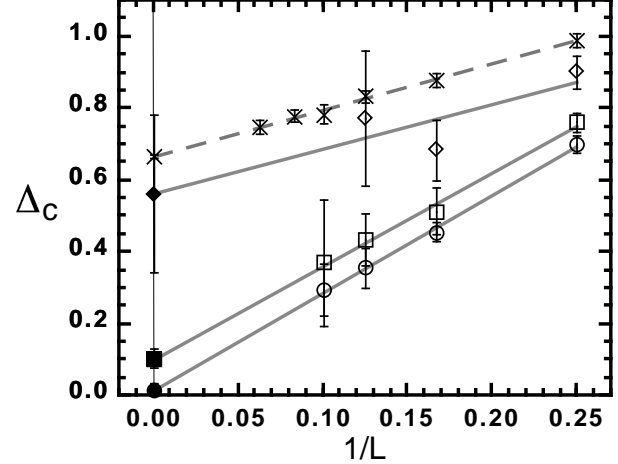


FIG. 1. System-size dependence of the charge gap amplitude at half filling. The circles, squares, and diamonds correspond to  $\tilde{U} = 3, 4$ , and  $5$ , respectively. The data are fitted by  $1/L$  and the extrapolated values to  $L \rightarrow \infty$  are plotted as the filled symbols. The crosses show the data on the ordinary Hubbard model at  $U = 4$ .<sup>64</sup>

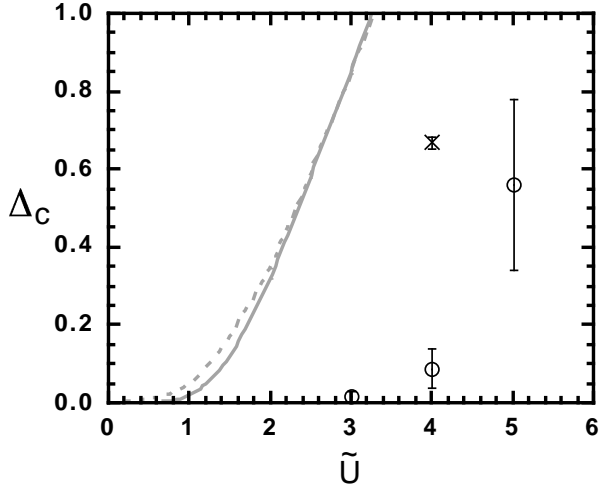


FIG. 2.  $\tilde{U}$  dependence of the charge gap amplitude in the thermodynamic limit. The circles and cross show the QMC data on the present model and on the ordinary Hubbard model at  $\tilde{U} = U^{64}$ , respectively. The gray and dotted curves are the mean-field results for the present model and the ordinary Hubbard model, respectively.

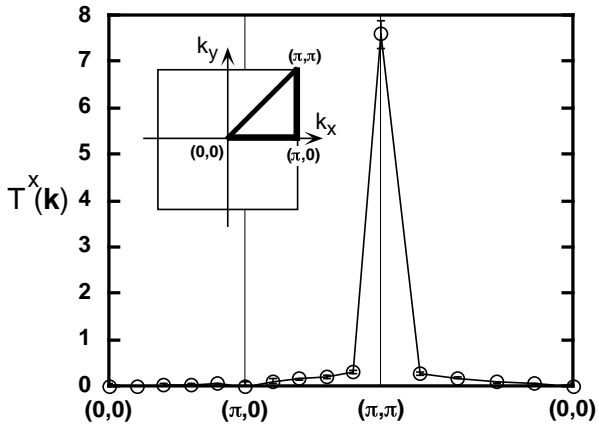


FIG. 3. The orbital correlation function ( $x$  component) at  $\tilde{U} = 4$  in the system with  $N_S = 10 \times 10$  at half filling. The data are presented along the bold line in the  $k$  space as shown in the inset.

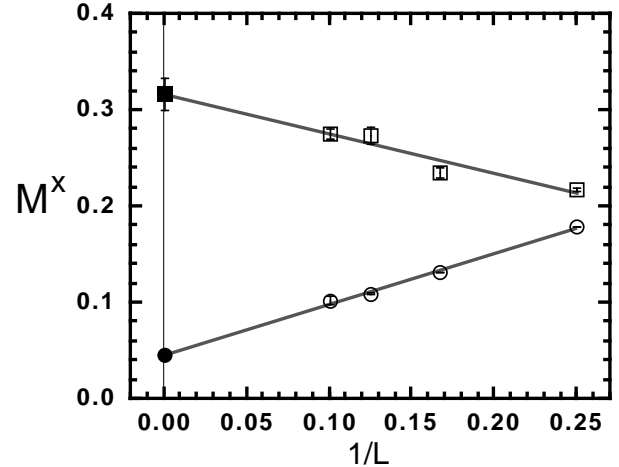


FIG. 4. System-size dependence of the moment of the orbital polarization at half filling. The circles and squares are for  $\tilde{U} = 3$  and 4, respectively. The data are fitted by  $1/L$  and the extrapolated values to  $L \rightarrow \infty$  are plotted as the filled symbols.

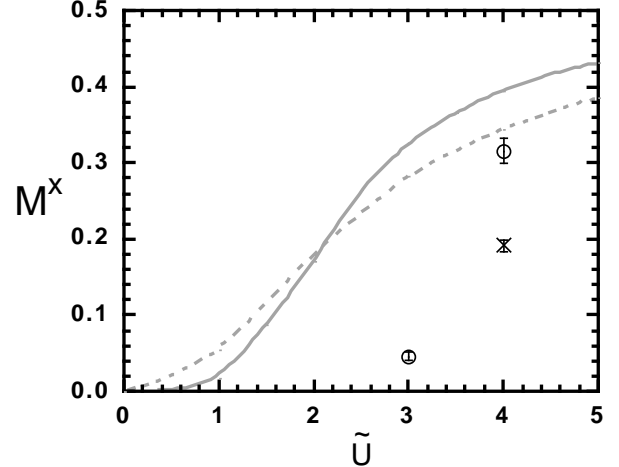


FIG. 5.  $\tilde{U}$  dependence of the long-ranged order of the orbital polarization in the thermodynamic limit. The circles and cross show the QMC data on the present model and for the ordinary Hubbard model at  $\tilde{U} = U^{49}$ , respectively. The gray and dotted curves results for the present model and for the long-ranged antiferromagnetic order of the ordinary Hubbard model, respectively.

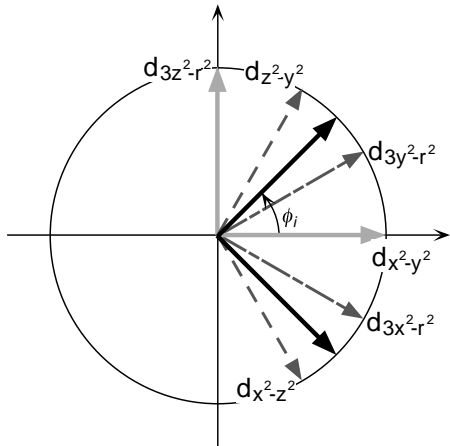


FIG. 6. Single-site orbital state defined as Eq. (16). The gray arrows at  $\phi_i = 0$  and  $\pi/2$  show the original basis in the Hamiltonian,  $d_{x^2-y^2}$  and  $d_{3z^2-r^2}$ , respectively. The bold black arrows at  $\phi_i = \pm\pi/4$  correspond to the pattern of the orbital ordering induced by the Coulomb interaction in our calculations. The other arrows show the basis at  $\phi_i = \pm\pi/6$  and  $\pm\pi/3$ . See the text for details.

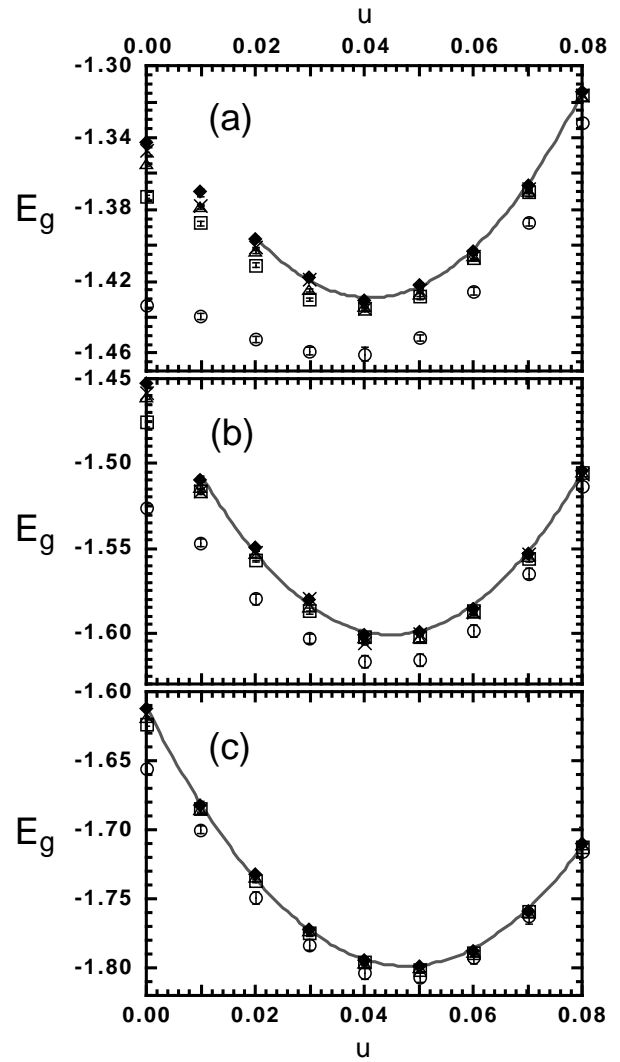


FIG. 7.  $u$  dependence of the ground state energy at half filling; (a)  $\tilde{U} = 3$ , (b)  $\tilde{U} = 4$  and (c)  $\tilde{U} = 5$ . We take  $g = 10$  and  $k = 100$ . The circles, squares, triangles, crosses, and diamonds correspond to the data for  $L = 4, 6, 8, 10$ , and  $\infty$ , respectively. The data for  $L = \infty$  are obtained by the extrapolation shown in Fig. 8. The curves show the fits by Eq. (18) for the data for  $L = \infty$ .

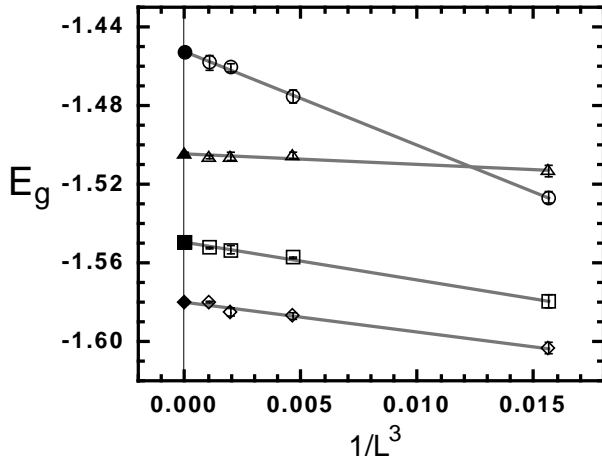


FIG. 8. System-size extrapolation of the ground state energy for  $\tilde{U} = 4$  at half filling. The circles, squares, diamonds, and triangles correspond to the data for  $u = 0.0, 0.02, 0.03$ , and  $0.08$ , respectively. The data are fitted by  $1/L^3$  and the extrapolated values to  $L \rightarrow \infty$  are plotted as the filled symbols.

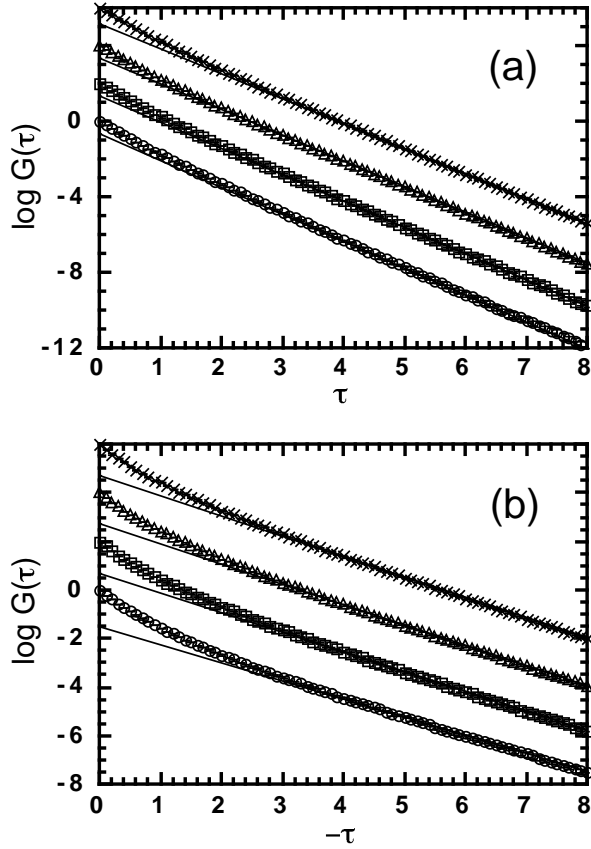


FIG. 9. Imaginary-time dependence of the uniform Green's function for the ground state at  $\tilde{U} = 3$ ,  $g = 10$ , and  $k = 100$ : (a)  $\tau > 0$  and (b)  $\tau < 0$ . The circles, squares, triangles, and crosses correspond to the data for  $L = 4, 6, 8$ , and  $10$ , respectively. Note that the origin for the  $\log G(\tau)$  has an offset to distinguish the data for each system size in both figures. The lines are the fits to the exponential tails to calculate the charge gap amplitude.

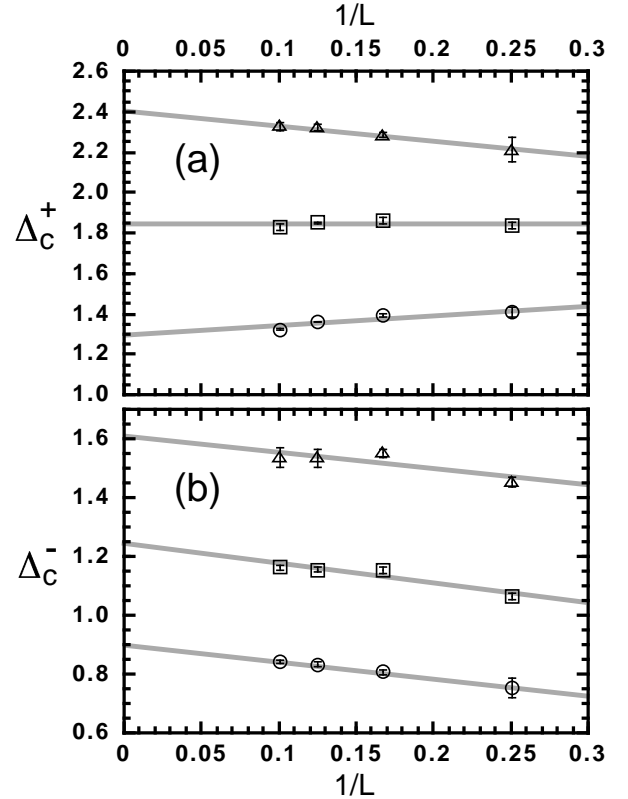


FIG. 10. System-size dependence of the charge gap amplitude for (a) electron doping and (b) hole doping. The circles, squares, and triangles correspond to the data at  $\tilde{U} = 3, 4$ , and  $5$ , respectively. The lines are the fits of  $1/L$ .

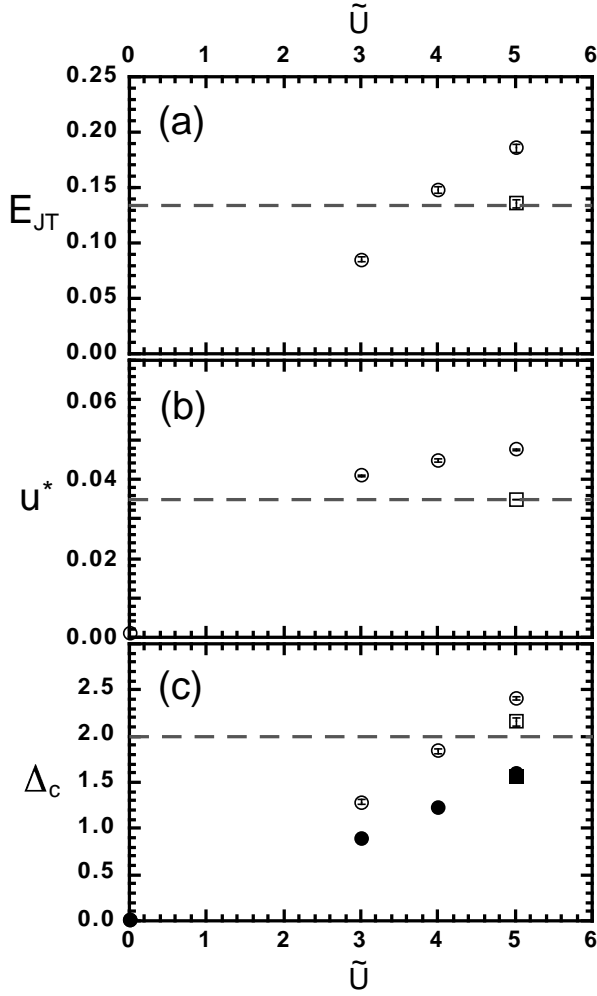


FIG. 11.  $\tilde{U}$  dependence of (a) the stabilization energy of JT distortions, (b) the amplitude of oxygen distortions, and (c) the charge gap amplitude. We take  $g = 10$  and  $k = 100$ . In (c), the open (filled) symbols denote the charge gap for the electron (hole) doping. The dotted lines show the experimental results of the corresponding quantities. The squares denotes the data at  $g = 10$  and  $k = 130$ . See the text for details.

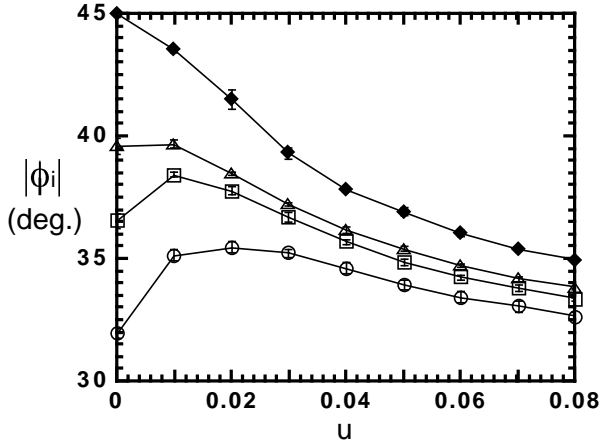


FIG. 12.  $u$  dependence of the angle  $\phi_i$  defined in Eq. (16). We take  $\tilde{U} = 4$ ,  $g = 10$ , and  $k = 100$ . The circles, squares, triangles, and diamonds correspond to the data for  $L = 4, 6, 8$ , and  $\infty$ , respectively. The lines connecting the data are guides to eye.

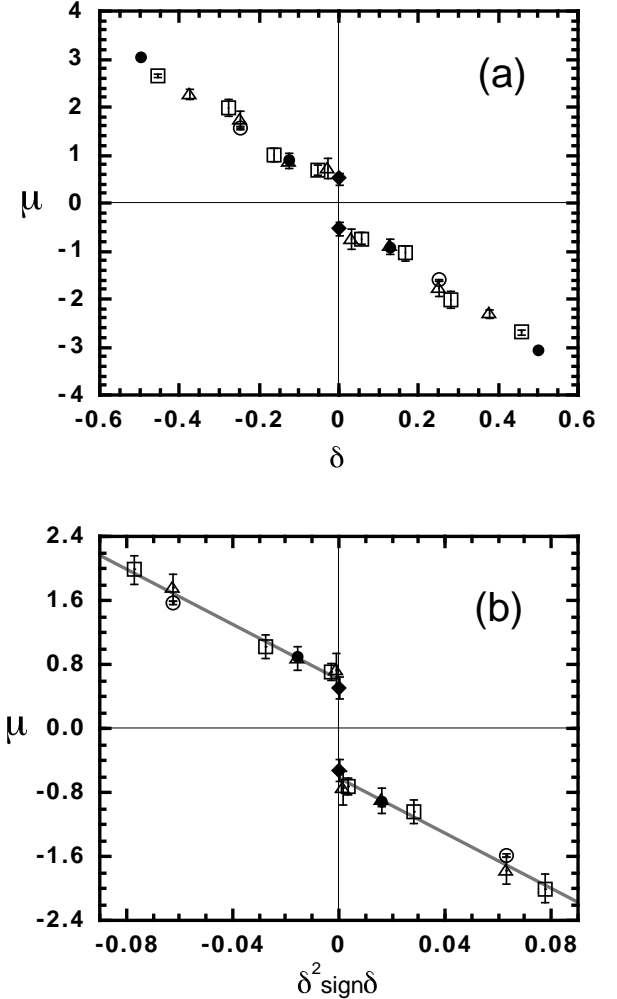


FIG. 13. Doping dependence of the chemical potential for  $\tilde{U} = 5$ . The open circles, squares, and triangles correspond to the data for  $L = 4, 6$ , and  $8$ , respectively. The solid circles are the data for  $L = 4$  with the periodic boundary condition. The solid diamonds at  $\delta = 0$  show the charge gap amplitude obtained in Fig. 2. The data are fitted by  $\delta^2$  in (b).

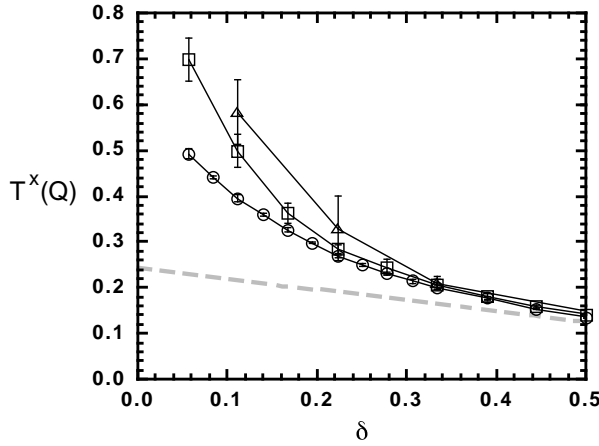


FIG. 14. Doping dependence of the peak values of the orbital correlation function for  $N_s = 6 \times 6$ . The circles, squares, and triangles correspond to the data for  $\tilde{U} = 3, 4$ , and  $5$ , respectively. The dotted line shows the result for the noninteracting case. The lines connecting the data are guides to eye.

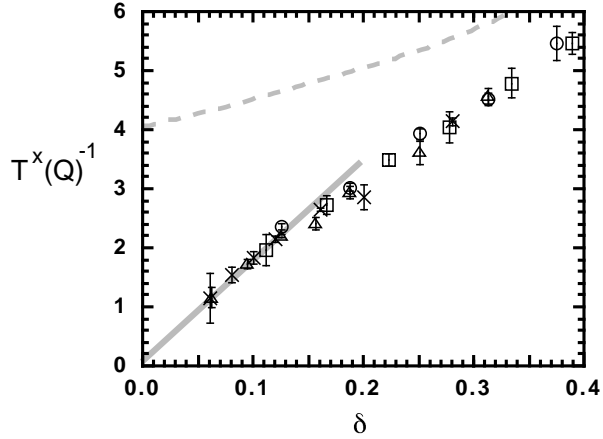


FIG. 15. Doping dependence of the inverse peak values of the orbital correlation function for  $\tilde{U} = 4$ . The circles, squares, triangles, and crosses correspond to the data for  $L = 4, 6, 8$ , and  $10$ , respectively. The gray line shows the fit by a  $\delta$ -linear function for  $0 < \delta < 0.15$ . The dotted line shows the result for the noninteracting case.

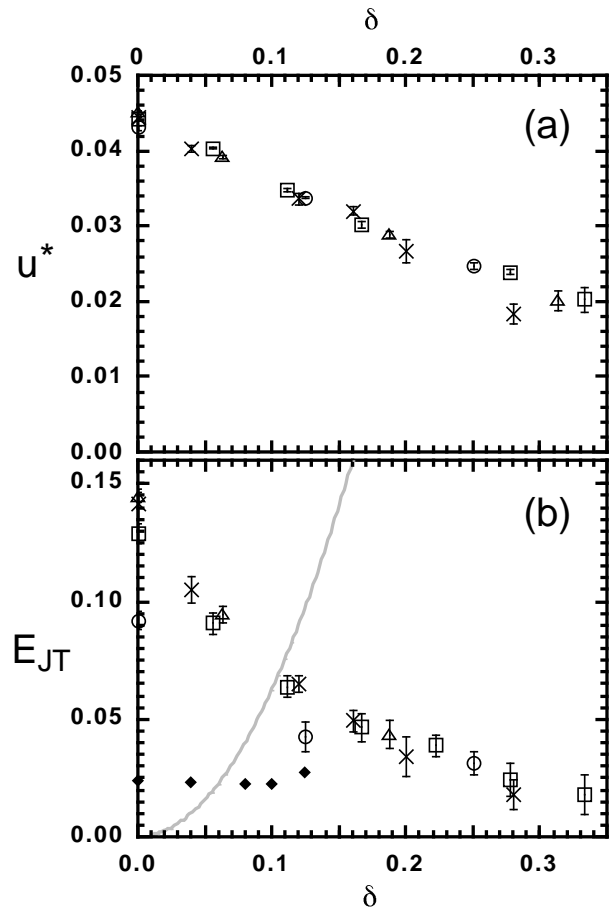


FIG. 16. The JT distortion in the hole-doped region for  $\tilde{U} = 4$ ,  $g = 10$ , and  $k = 100$ ; (a) the oxygen distortion and (b) the stabilization energy. The circles, squares, triangles, and crosses correspond to the data for  $L = 4, 6, 8$ , and  $10$ , respectively. The filled diamonds in (b) are the magnetic transition temperature in experiments. The gray curve shows the estimation of the kinetic-energy gain in the  $z$  direction given by Eq. (14).

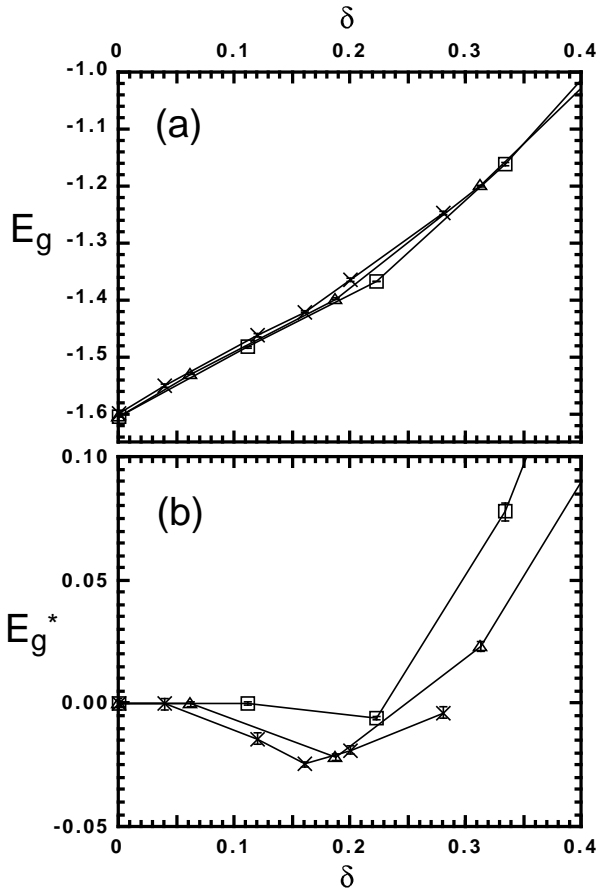


FIG. 17. Doping dependence of the ground state energy per site for  $\tilde{U} = 4$ ,  $g = 10$ , and  $k = 100$ . The squares, triangles, and crosses correspond to the data for  $L = 6, 8$ , and 10, respectively. The lines are guides to eye. In (b), the quantity defined in Eq. (23) is plotted to show the convex region clearly. See the text for details.

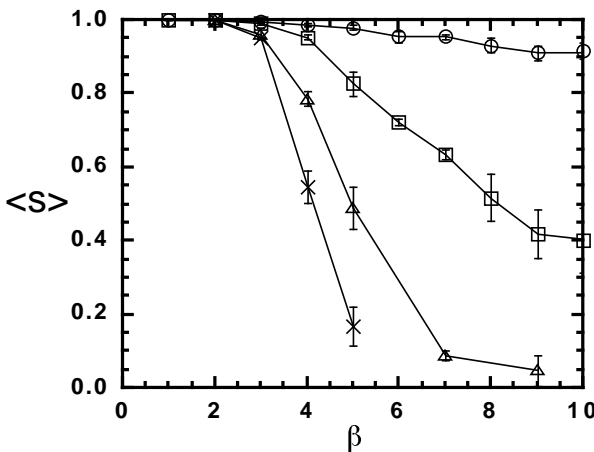


FIG. 18.  $\beta$  dependence of the negative sign for  $\tilde{U} = 4$  and  $g = 0$  at half filling. The circles, squares, triangles, and crosses correspond to the data for  $L = 4, 6, 8$ , and 10, respectively. The orbital-singlet state is used as the trial wave function. The lines are guides to eye.

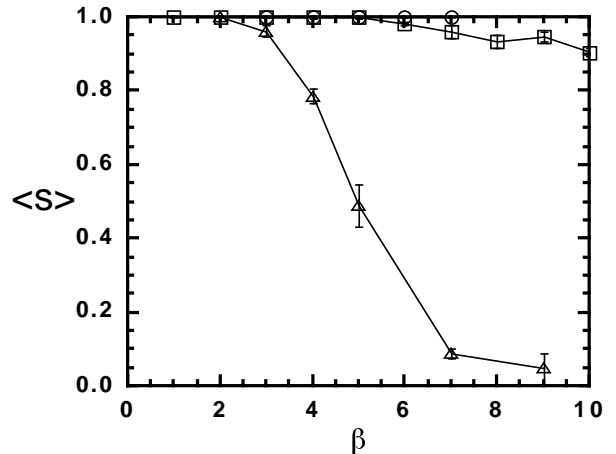


FIG. 19.  $\beta$  dependence of the negative sign for  $N_S = 8 \times 8$  at half filling with  $g = 0$ . The circles, squares, and triangles correspond to the data for  $\tilde{U} = 2, 3$ , and 4, respectively. The orbital-singlet state is used as the trial wave function. The lines are guides to eye.

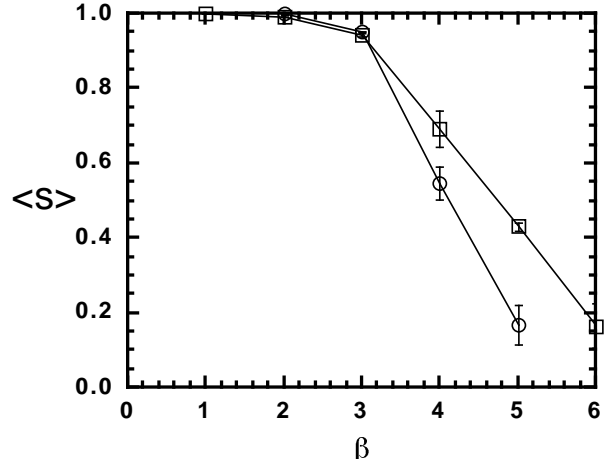


FIG. 20.  $\beta$  dependence of the negative sign for  $\tilde{U} = 4$  and  $g = 0$  in the system with  $N_S = 10 \times 10$  at half filling. The circles and squares correspond to the data on the orbital-singlet wave function and on the unrestricted Hartree-Fock solution with  $\tilde{U} = 2.1$ , respectively. The lines are guides to eye.

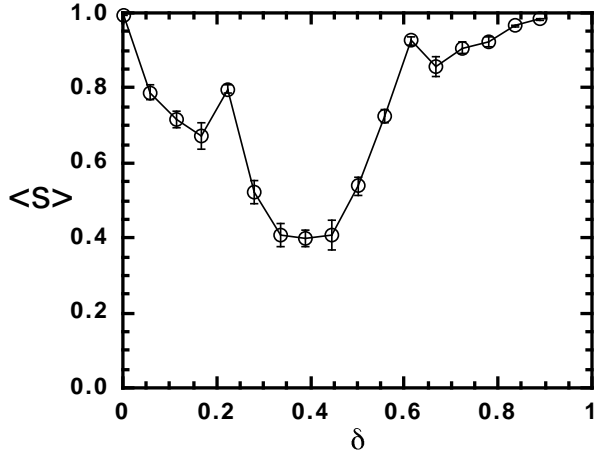


FIG. 21. Doping dependence of the negative sign at  $\beta = 5$  for  $\tilde{U} = 3$  and  $g = 0$  in the system with  $N_s = 6 \times 6$  for the choice of the orbital-singlet trial functions. The lines are guides to eye.

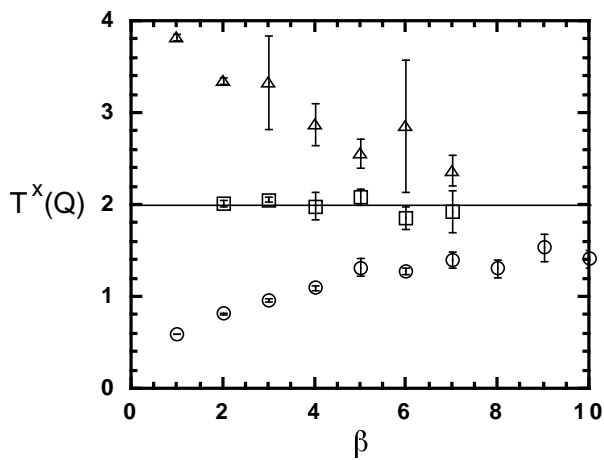


FIG. 22. Convergence for  $\beta$  of the orbital correlation function at the peak point for  $\tilde{U} = 4$  and  $g = 0$  in the system with  $N_s = 6 \times 6$  at half filling. The circles, squares, and triangles correspond to the data obtained from the orbital-singlet wave function, the unrestricted Hartree-Fock solution with  $\tilde{U} = 2.4$  and 3, respectively. The horizontal line shows the converged value.

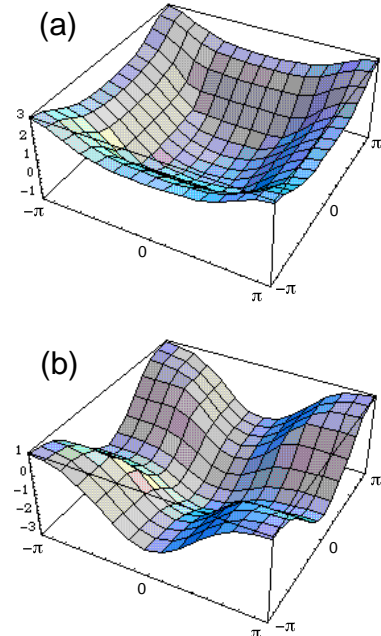


FIG. 23. Energy dispersions for the noninteracting system defined in Eq. (B5); (a)  $\varepsilon_+$  and (b)  $\varepsilon_-$ .

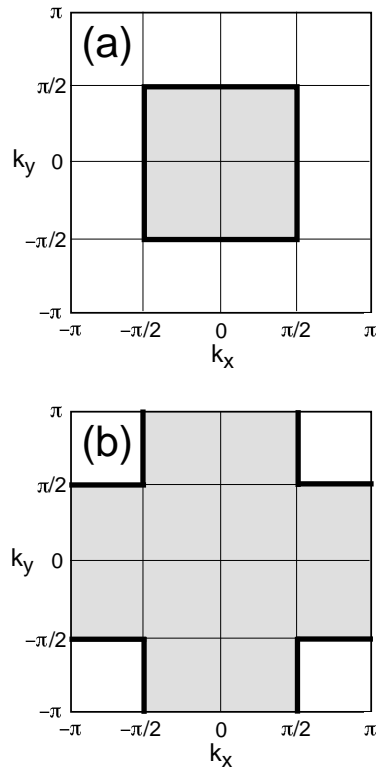


FIG. 24. Fermi surfaces in the noninteracting system at half filling; (a) for the branch  $\varepsilon_+$  and (b) for  $\varepsilon_-$ . The bold solid lines show the Fermi surfaces and the shaded regions inside them are the occupied states.

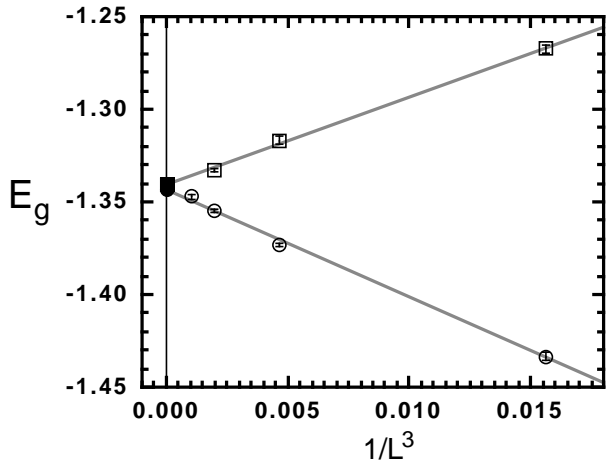


FIG. 25. System-size extrapolation of the ground state energy for  $\tilde{U} = 3$  and  $g = 0$  at half filling. The circles are the data on the series of  $L = 4n$  with the antiperiodic boundary condition or  $L = 4n + 2$  with the periodic boundary condition. The squares are the data on the series of  $L = 4n$  with the periodic boundary condition or  $L = 4n + 2$  with the antiperiodic boundary condition. The data are fitted by  $1/L^3$  and the extrapolated values to  $L \rightarrow \infty$  are shown as the filled symbols.